Edge-localized-modes (ELMs) in tokamaks

A.W. Leonard

General Atomics, PO Box 85608, San Diego, CA 92186-5608, USA

Abstract. Edge-localized-modes (ELMs) are a ubiquitous feature of H-mode in tokamaks. When gradients in the H-mode transport barrier grow to exceed the MHD stability limit the ELM instability grows explosively rapidly transporting energy and particles onto open field lines and material surfaces. Though ELMs provide additional particle and impurity transport through the H-mode transport barrier, enabling steady operation, the resulting heat flux transients to plasma facing surfaces project to large amplitude in future low collisionality burning plasma tokamaks. Measurements of the ELM heat flux deposition onto material surfaces in the divertor and main chamber indicate significant broadening compared to inter-ELM heat flux, with a timescale for energy deposition that is consistent with sonic ion flow and numerical simulation. Comprehensive ELM simulation is highlighting the important physics processes of ELM transport including parallel transport due to magnetic reconnection and turbulence resulting from collapse of the H-mode transport barrier. Encouraging prospects for ELM control and/or suppression in future tokamaks include intrinsic modes of ELM free operation, ELM triggering with frequent small pellet injection and the application of 3D magnetic fields.

PACS Nos: 52.55.Fa, 52.55.Tn, and 52.55.Rk

I. Introduction

From the initial observation of the high confinement regime (H-mode) in the tokamak this mode of operation has been accompanied by periodic bursts of ejected plasma labeled edge-localized-modes (ELMs).[1,2] Many of the important aspects of ELM are highlighted in the discharge from DIII-D shown in Fig. 1. With additional heating, a spontaneous transition to H-mode results in an edge transport barrier with growing gradients in density and temperature just inside the last closed flux surface (LCFS), or separatrix in diverted tokamaks. This transition results in a large increase in global stored energy and confinement, primarily from an increase in the edge pressure. The edge pressure and its associated gradients grow until an MHD limit is reached. The resulting ELM instability causes a rapid relaxation of the edge pressure with a burst of heat flux flowing into the divertor. After the ELM burst relaxes the edge pressure, the H-mode transport barrier is re-established allowing the edge pressure and its gradients to build toward the next ELM.

The ELM has several important implications for the H-mode operational regime in future burning plasma tokamaks. First the ELM provides density, and particularly impurity control for the core plasma. The H-mode barrier is particularly effective at confining fuel ions and impurities within the core plasma.[3] This becomes a problem as accumulating impurities eventually lead to a radiative collapse of the plasma discharge, and in a burning plasma would also dilute the core plasma fuel. The ELM provides a mechanism for flushing these impurities through the H-mode transport barrier. On the deleterious side, the ELM burst transports a heat flux transient to plasma facing components (PFCs), particularly in the divertor, but also to the main chamber walls. In future larger burning plasma tokamaks, where the plasma stored energy normalized by surface area will be significantly larger than in current devices, the ELM heat flux burst represents a significant risk of damage to PFCs. Another implication of the ELM is the potential for coupling to, or triggering, other MHD instabilities such as the Resistive Wall Mode (RWM) or Neoclassical Tearing Mode (NTM).[4,5]

Developing a predictive capability for the ELM instability involves a broad cross-section of fusion plasma physics. The ELM story begins with the physics of the H-mode and the spontaneous transport barrier formation with steep gradients in both temperature and density. It includes ideal MHD with limits to pressure and current gradients. It continues with nonlinear MHD evolution and magnetic reconnection due to anomalous current diffusion. It proceeds with radial transport of heat and particles due to turbulence and parallel transport along magnetic field lines. It finally results in plasma-material interaction with the deposition of heat and particles on material surfaces with sheath effects in turn constraining plasma transport.

In this paper, we review the current understanding of the ELM instability, and our capability to predict ELM characteristics in future devices. Of particular focus is the ELM deposition of particles and heat flux to material surfaces, as this represents the most significant risk of the ELM to future tokamak design and operation. A detailed understanding and predictive capability for the ELM instability serves not only as a projection of expected transients, but also as a guide for the development of ELM mitigation and control capabilities. In Sec. II, we begin with a review of the H-mode characteristics that lead to an ELM. Particular focus is given to the aspects of the edge gradients that drive the ELM instability. The linear onset conditions for the ELM are summarized. In Sec. III, we review experimental observations of ELM transport, from losses of density and temperature from the core plasma, to their transport through the open field lines of the scrape-off-layer (SOL), to their final deposition on material surfaces. Section IV summarizes transport of the ELM energy and particles to the divertor. Section V describes transport of ELM energy to the main chamber walls via radially propagating filaments. In Sec. VI, progress in the development of comprehensive computational models of the ELM is summarized. Comparisons with experimental observations are made, along with highlighting areas in need of further development. In Sec. VII, the scaling of experimental observations is projected to future devices with the implications explored. The impact of ELMs in ITER is summarized as ITER is the first device where ELMs will represent a significant risk to in-vessel components. In Sec. VIII, current understanding of the ELM instability is used as a guide to briefly describe efforts to develop ELM control and mitigation schemes. Finally in Sec. IX, we conclude with a summary of current understanding of the ELM instability and highlight areas where future work would be of particular benefit.

II. H-mode profiles and ELM stability

The H-mode transport barrier results in growing edge gradients that eventually become unstable to the ELM MHD instability. The physics of the H-mode and the conditions required to achieve the H-mode transition are summarized elsewhere.[6-8] The enabling feature of the H-mode transport barrier is a sheared perpendicular rotation profile, driven by a radial electric field, $E_r \times B$, in the plasma edge, as shown in Fig. 2, which suppresses the long wavelength turbulence of L-mode. The characteristic shape of the rotation profile shown in Fig. 2 has given rise to the label "E_r well". The transport barrier created by the E_r well leads to steep gradients in the edge density and temperature profiles, with a typical example from DIII-D shown in Fig. 3. The ion temperature gradient also steepens during the H-mode, but typically to a lesser extent than the electron temperature profile.[9] These steep edge profiles in a narrow layer inside the separatrix have been labeled the H-mode pedestal as the core density and temperature profiles rest on top of them.

Another important feature of the H-mode profiles in regards to MHD stability is the current driven by the pressure gradient, or so-called bootstrap current.[10,11] An example of the calculated flux-surface-averaged bootstrap current driven by the typical edge pressure gradient of Fig. 3, is shown in Fig. 4. Model calculations of the bootstrap current have grown in sophistication to take into account the short scale lengths on the order of the poloidal gyro-radius that typify the edge pedestal.[12,13] Experimental confirmation of the bootstrap current has been made by parallel electric field analysis,[14] and direct measurement of the poloidal field profile.[15,16] Currently these measurement techniques have confirmed the bootstrap current model calculations to within ~20%.

The stability of the edge pedestal profiles can be expressed by a perturbed energy equation,

$$\delta W = \frac{1}{2}\int dV\left(\left|B_{1,\perp}\right|^2 + B_0^2\left|\nabla\cdot\xi_\perp + 2\xi_\perp\cdot\kappa\right|^2 + \lambda p_0\left|\nabla\cdot\xi\right|^2\right)$$
$$-\int dV\left(2\left(\xi_\perp\cdot\nabla p_0\right)\left(\kappa\cdot\xi_\perp\right) + J_{0,\parallel}\left(\xi_\perp\times B_0/B_0\right)\cdot B_{1,\perp}\right) \quad , \qquad (1)$$

where $B_{1,\perp}$ is the magnetic field perturbation, and $\xi_\perp$ is the fluid displacement perturbation.[17] The negative destabilizing terms represent the pressure gradient and parallel current drivers of the instability. Stabilizing terms include field line bending and compression of plasma fluid and magnetic field.

Sophisticated computational tools [18-21] have been developed to calculate the pedestal stability of Eq. (1) for reconstructed magnetic equilibria with experimentally realistic pressure and current profiles, such as those shown in Figs 3 and 4. These calculations find that for high toroidal mode number, $n > 20$, ideal ballooning modes driven by the pressure gradient can achieve second stability access due to the bootstrap current lowering the magnetic shear in the region of high pressure gradient. In turn the current driven peeling modes are stabilized by higher pressure. However, at finite values of n, typically 8–20, the peeling and ballooning models couple and close off access to the second stability region. The resulting stability space for the H-mode pedestal is conceptually presented in Fig. 5 as a function of pedestal current versus pedestal pressure gradient. At high density, the high collisionality in the pedestal suppresses the bootstrap current such that the pressure limit is set by higher n ballooning stability limit shown at the right hand side of the stability diagram. At low density and collisionality, the bootstrap current is fully expressed and current driven peeling modes limit the pedestal along the top of the stability diagram. Experimental confirmation of the calculated stability limit has come by observations of ELM onset for measured pedestal pressure gradients consistent with crossing the stability boundary within experimental uncertainty of the measured pedestal pressure gradient and modeled bootstrap current, typically ≤20%. A multi-machine study, Fig. 6, carried out by the International Tokamak Physics Activity (ITPA) pedestal topical group found good agreement across multiple tokamaks while utilizing several different computational tools.[22]

The maximum attainable stable pressure is typically at moderate normalized density, $\bar{n}_e/n_{GW} \sim 0.5$ [Greenwald density limit, $n_{GW}\left(\times 10^{19}\right) = I_p(\mathrm{MA})\big/\pi a^2(\mathrm{m})$], where coupled peeling-ballooning modes of moderate toroidal mode number, n = *8–15*, limit the pedestal. The limits for an individual discharge depend on a number of parameters such as the plasma shape, beta, safety factor q, plasma density and pedestal width. With the additional assumption of the local pedestal pressure gradient set by the Kinetic Ballooning Mode (KBM), the EPED model has been developed to successfully provide quantitative predictive capability for the pedestal pressure limit.[23] This understanding and development of computational tools for the ELM stability limit has greatly aided the optimization of tokamak discharge control parameters for obtaining maximum performance in existing devices, and the optimization of future tokamak design and operation.

Finally, linear stability analysis predicts the spatial structure of the ELM instability at its onset. In Fig. 7 is shown a 2D contour plot of the displacement amplitude from stability analysis with the ELITE code from a realistic set of experimental conditions.[24] Several visible features of the eigenmode structure are common across a range of conditions. Though only the $n = 10$ toroidal mode is shown in Fig. 7, a range of toroidal mode numbers maybe unstable at the ELM onset. The most unstable toroidal mode number usually increases with density and collisionality as the mode becomes more ballooning-like. The eigenmode peaks in amplitude at the outer midplane, as would be expected in this region of bad magnetic curvature. The amplitude is also small near the X-point, though the stabilizing poloidal field is very low in this region. This is due to the stabilizing influence of increased magnetic shear in this region. Finally, the radial extent of the eigenmode corresponds to the region of high pedestal pressure gradient and high current density. The region of instability extends somewhat further into the core plasma at lower density with a higher bootstrap current. With these characteristics, the ELM instability would be expected to consist of multiple modes over a range of toroidal mode number, n, concentrated at the outer midplane, and involving most of the pedestal. In the next section, the role of these features of the linear mode analysis will be examined in the experimental data.

III. Pedestal ELM losses

Once the pedestal linear MHD stability limit is exceeded the instability grows rapidly and nonlinearly. When this instability is large and periodic, it is known as a “Type I” ELM.[25] Under certain conditions smaller and/or irregular edge localized bursts may occur that have been given a variety of classifications. Those instabilities will be briefly described in Sec. VIII. This review is primarily concerned with the physics of the larger Type I ELMs that are of more serious concern for future devices. A typical example of the pedestal evolution at an ELM is shown from JET in Fig. 8.[26] The magnetic perturbation, from Mirnov signals, grows very rapidly, ~10 μs, within a few 10’s of Alfvèn times. The magnetic signature is turbulent and often without a distinguishable precursor. However, careful dedicated measurements have detected ELM precursors in magnetic signals[27-30] and with electron cyclotron emission imaging (ECEI),[31] exhibiting toroidal mode numbers that are expected from linear MHD stability analysis as described in the previous section. During the instability the magnetic signals are turbulent, indicating the ELM’s fully developed nonlinear character, though coherent structures are observed in visible light at the plasma edge with $n \sim 8-20$ toroidal mode structure, again consistent with linear stability analysis.[32,33] The duration of the instability is usually ~200 μs, with only modest variation across conditions and devices.[26] During this phase pressure is lost from the pedestal as evidenced by the drop in edge electron temperature, T_e, and soft x-ray (SXR) signal in Fig. 8. The divertor x-ray signal of hot electrons and D_α signal for divertor ion flux show the plasma lost from the pedestal being transported to the divertor.

While the total energy lost at an ELM is often measured with a fast diamagnetic loop diagnostic, the individual components of density and temperature loss are characterized by a variety of diagnostics, including Thomson scattering for electron density and temperature, microwave reflectometry for electron density, electron cyclotron emission (ECE) for electron temperature and charge exchange recombination (CER) spectroscopy for ion temperature.[34-37] An example of the electron density and temperature profiles just before and after an ELM in DIII-D, Fig. 9, is produced from Thomson scattering, using ELM synchronized averaging over a period of constant conditions. The profiles exhibit a loss of plasma that peaks in the steep gradient region, but also extends into the plasma core as shown by the fraction losses in Fig. 9(c) and Fig. 9(d). Similar loss profiles of pedestal electron density and temperature have also been measured by microwave reflectometry and ECE diagnostics respectively on a number of other tokamaks.[38-41] The relative size of the ELM drop may vary as will be examined later in this review.

The effect on the ions due to an ELM has been characterized with fast CER measurements of the carbon impurity CVI.[37,42] The ion temperature loss, ΔT_{i}, at an ELM is seen to be similar to that for T_{e}, as shown in Fig. 10, dropping by up to 50% at the top of the pedestal. The drop extends into the core plasma in a similar fashion as for T_{e}. Another important ion characteristic that is affected by an ELM is the rotation profile, also shown in Fig. 10. Both the toroidal and poloidal rotation profiles are flattened to essentially zero at the ELM. The flattening of the rotation profile results in a reduction, or even elimination, of the E_{r} well, or $E_{\mathrm{r}} \times B$ shear profile, as shown in Fig. 11, thought responsible for the H-mode transport barrier. After several hundred milliseconds, at the end of the turbulent phase, the E_{r} well begins building again towards the next ELM. An important aspect of the time dependence of the ion profile evolution at an ELM (Fig. 9 of Ref. 37) is that the rotation profile, and E_r well, immediately flatten, within ~100 μs, with the drop in T_i following after the E_r well has collapsed. A similar timescale for the loss of electron thermal energy, show in Fig. 8, indicates that one possibility for the ELM thermal transport is the loss of the transport barrier resulting in rapid turbulent transport of heat.

The loss of pedestal plasma described above has been shown to originate at the outer midplane. Fast microwave reflectometry diagnostics have successfully reconstructed the pedestal density profile evolution through an ELM.[40,43] On ASDEX-Upgrade, complementary reflectometry systems probe both the high-field-side (HFS) and low-field-side (LFS) pedestals to produce a density profile every 25 μs.[40] An example of the change in the LFS density profile produced by reflectometry at an ELM is shown in Fig. 12. While the HFS profile is seen to behave in a qualitatively similar manner, the response is delayed from the LFS perturbation. The delay has been quantitatively correlated with the ion parallel transport time from the HFS to LFS midplane, as shown in Fig. 13. Here the ion transport time is calculated as $\tau_{||} = \pi R q / c_{s,ped}$ where $c_{s,ped} \sim \sqrt{\left(T_{e,ped} + T_{i,ped}\right) / m_i}$ and πRq is the connection length from the LFS to HFS midplane across the top of the plasma (opposite of the X-point). This data indicates plasma density is first lost at the LFS midplane with sonic flow parallel to the magnetic field from the HFS to equalize the density on a flux surface. Similar behavior has been observed in JT-60U with vertical far infrared (FIR) interferometer chords where the density perturbation is first observed at the LFS with propagation to the HFS at the parallel ion sound speed.[44] A further confirmation of the LFS midplane source for ELM transport comes from divertor measurement of D_α signals of recycling ion flux in the inboard and outboard divertors.[26,35,44,45] At an ELM, the rise in HFS divertor D_α is delayed from the LFS divertor by the difference in ion sound speed connection times from the HFS midplane. And finally additional evidence is provided at DIII-D where in a magnetically balanced double-null configuration (DN) with the LFS and HFS SOLs magnetically disconnected, ELM fluxes arrive only at the LFS upper and lower divertors.[46] The in/out asymmetry measurements consistently indicate the ELM transport of heat and particles occurs across the LFS separatrix, consistent with linear stability analysis indicating the highest instability amplitude at the LFS, in the bad magnetic curvature region.

The size of an ELM, or the total energy and particles lost from the core plasma, determines the potential for damage to material surfaces. Understanding what controls the magnitude of this loss would aid greatly in extrapolating current results to future devices. The energy lost at an ELM is typically normalized by the pedestal energy when comparing relative ELM sizes across devices of varying size. Here pedestal energy, $W_{\rm ped}$, is given by $W_{\rm ped} = \frac{3}{2} n_{\rm ped}\left(T_{\rm e,ped} + T_{\rm i,ped}\right)V_{\rm plasma}$ where the pedestal values are those at the top of the pedestal and $V_{\rm plasma}$ is the volume of plasma inside the separatrix. Under similar conditions the relative ELM size, $\Delta W_{\rm ELM}/W_{ped}$, is roughly constant across a range of device sizes.[47] This is not a surprising result as the energy available for transport is proportional to the pedestal pressure and the volume of the steep gradient pedestal region. The pedestal volume is typically proportional to the total plasma volume as studies have found the pedestal to be proportional to device minor radius.[23]

The discharge characteristic most strongly affecting large Type I ELMs is the pedestal collisionality. An international multi-device database assembled by the ITPA Divertor/SOL Topical Group indicates that relative ELM size is strongly correlated with pedestal collisionality as shown in Fig. 14.[26] The database indicates that large ELMs, up to 20% of the pedestal energy, can be expected at low collisionality, υ^*_{ped}, such as that expected for ITER. At higher density and collisionality, near the density limit with additional fueling, $\bar{n}_e/n_{GW} \sim 1.0$, $\upsilon^*_{ped} \geq 1.0$, the ELM energy loss is much smaller, ≤5% of W_{ped}. Here pedestal collisionality is defined as $\upsilon^*_{ped} = Rq_{95}\varepsilon^{-3/2}\left(\lambda_{e,e}\right)^{-1}$ where $\lambda_{e,e}$ is the electron-electron Coulomb collision mean free path length. This neoclassial formulation of collisionality is characteristic of the pedestal bootstrap current, where $\upsilon^*_{\rm ped} \leq 0.1$ represents near full expression of the bootstrap current driven by the pressure gradient and $\upsilon^*_{\rm ped} \geq 1.0$ corresponds to suppression of the bootstrap current by a factor of 3 or more.[11]

The database of Fig. 14 indicates significant scatter in the ELM size at a fixed collisionality. And indeed, ELM size can vary significantly from ELM to ELM in a single discharge. A study in JET measured a 10% variation in ELM frequency and 15% standard deviation of energy loss of individual ELMs for constant conditions.[35] The level of ELM size scatter can vary with conditions with generally more scatter at low q_{95} and high collisionality.

The energy lost at an ELM can be separated into its convective (density loss) and conductive (temperature loss) components. This separation of transport channels has been used to examine the collisionality dependence of $\Delta W_{\rm ELM}$ in DIII-D as shown in

Fig. 15.[48] In this dataset, utilizing Thomson scattering with ELM synchronized averaging, the fractional conductive losses steadily decrease towards zero at high density and collisionality with additional gas puff fueling to near the Greenwald density limit $\left(n_{\mathrm{GW}} = I_{\mathrm{p}} / \pi a^2\right)$. The fractional conductive losses are correlated with normalized density even though the plasma current variation in this data set produced a factor of two or more variation in pressure at the top of the pedestal. On DIII-D the loss of ion temperature, as measured by CER, at an ELM follows the same trend as the electron temperature.[37] In contrast the convective losses, though with substantial scatter, exhibit no consistent trend with density and collisionality. An ELM study on JET exhibited a similar trend with the pedestal conductive losses measured with ECE dropping to near zero at high density with convective losses only weakly affected.[26] Additionally the JET study found the shape of the temperature drop, peaking in the high gradient region, to remain fixed with density, with only its magnitude decreased. In other words, the ELM affected volume did not change with density, rather the relative contribution of thermal conduction was suppressed at high density and collisionality.

Linear MHD stability analysis of the DIII-D dataset of Fig. 15 provides some insight into the ELM loss mechanism and its dependence on collisionality. Stability analysis with the ELITE code was performed at low, moderate and high density on this dataset with magnetic equilibrium reconstruction using the measured pressure gradient and the Sauter model for the bootstrap current.[49] For the low density case with the pedestal bootstrap current near fully expressed, the unstable eigenmode growth rate peaked at a toroidal mode number of $N \sim 18$. At high density the edge bootstrap current was near completely suppressed with the unstable modes peaking for $n \geq 50$. It can be speculated that at low collisionality, and high edge bootstrap current, the current driven aspect of the ELM leads to magnetic reconnection and ergodization of field lines allowing fast parallel conduction of heat from the pedestal onto open field lines. At high density and low edge current, the ELM becomes exclusively ballooning in character with interchange type transport that does not involve magnetic reconnection and magnetic field line ergodization with its associated parallel conduction. Testing this hypothesis will require further development of simulation of nonlinear MHD evolution and transport that are described in Sec. VII.

IV. ELM transport into the divertor

Once core plasma energy and particles are transported by the ELM instability onto open field lines, they make their way quickly to the divertor target. The critical issue for PFCs is the pulse of heat flux that arrives at the divertor surface. An example of such a pulse can be seen in fast infra-red (IR) camera measurement of the JET MkII GB divertor,[50] as shown in Fig. 16. This figure exhibits characteristics common in most tokamaks with Type I ELM heat flux measurements. Plotted are both the surface temperature measurement and the inferred heat flux from a 2D thermal conduction model.[51] Before the ELM, the divertor surface temperature is slowly rising due to the steady-state divertor heat flux between ELMs. After the ELM onset the surface temperature rises quickly reaching a peak within a few hundred microseconds and then decaying with a timescale a factor of 2–3 greater than the rise. The surface heat flux, inferred from the temperature data, follows a similar pattern, peaking at about the same time.

In a 1D thermal conduction model with a constant power deposition, the surface temperature rise will be given by

$$\Delta T \propto \Delta W_{\mathrm{div}} \Big/ \left(A\sqrt{t} \right) \quad , \tag{2}$$

where ΔW_{div} is the total energy deposited in the divertor, and A is the area of deposition within time t. The three parameters of Eq. (2) are the key parameters to consider when evaluating the potential of ELMs to cause damage to material surfaces. Since it is the peak temperature that poses the primary risk for damage through melting of the divertor components, it is the energy that arrives before the peak that drives the ultimate peak surface temperature.

The first of the parameters of Eq. (2) to examine is the time of heat flux deposition to reach peak surface temperature. A multi-machine study using common analysis techniques found the rise time of the heat flux to be consistent with thermal ion transit from the pedestal into the divertor, parallel to the magnetic field.[26,52,53] Shown in Fig. 17 is τ_{IR} the time from the ELM onset to the peak surface temperature versus $\tau_{||} = 2\pi q_{95} R\sqrt{(T_e + T_i)/m_i}$ where the temperatures are characteristic of those in the middle of the pedestal and m_i is the mass of the main ions.

The correlation of heat flux rise time with parallel ion transport could be considered surprising given the fast time scale of electron thermal conduction. However, many of the features of the ELM divertor heat flux time dependence, shown in Figs 16 and 17, are found to be consistent with a kinetic model of parallel transport. To examine the relevant physics processes controlling the ELM divertor heat flux, particle-in-cell (PIC) kinetic simulations have been employed.[54-57] The standard 2D edge fluid code simulations are inadequate for this task in that they require flux limits to parallel conduction and must specify the sheath transmission factor carrying heat flux to the surface, which in practice is likely to be both spatially and temporally varying. In the PIC simulation shown in Fig. 18, the energy from a typical ELM in JET is released into a 1D geometry with the appropriate parallel path length midway between two targets.[56] The features of this simulation highlight the important physical processes that are expected to control ELM heat flux in current and future devices. At $t = 0$ the simulation injects plasma with the pedestal density and temperature over the characteristic ELM duration, ~200 μs, into a cooler lower density background SOL plasma. Within a few μsec, the faster electrons reach the target, carrying heat flux, but more importantly they raise the sheath potential, as evidenced by a factor of 3–4 increase in sheath transmission factor. The high sheath potential holds back further increases in heat flux until the slower injected ions make their way to the target. At that time, ~100 μs, the ions carry the bulk of the heat flux to the target as they accelerate through the sheath. After the instability terminates and energetic plasma is no longer injected into the SOL, the target heat flux reaches a peak and then begins to drop. This simulation recreates the experimental observations of the ELM heat flux rising on the timescale of the thermal ion transit time and decay a factor of 3–5 longer. Further the simulations indicate that only ~30% of the ELM energy arrives before the peak in target power and surface temperature, in agreement with experimental measurements,[52,56] such as that shown in Fig. 16. It is this 30% of the deposited ELM energy that drives the risk for melting of divertor target surfaces. These simulations lend confidence to the empirical scaling of ELM deposition time from current tokamaks to future larger tokamaks.

The other factor necessary for predicting the surface temperature rise is the ELM energy deposited per unit area. The empirical scaling of this parameter has been examined in terms of (a) the fraction of total ELM energy deposited on the divertor target, (b) splitting of the deposited ELM energy between the inboard and outboard divertor targets, and (c) the area over which the ELM energy is deposited in each divertor. The first factor, the divertor deposited ELM fraction has been measured in several devices and found to vary from ~50% for large ELMs of 20% of W_{ped}, to ≥90% for small ELMs of ≤10% of W_{ped}. [47,52,58,59] The divertor ELM energy fraction from JET shown in Fig. 19 is typical of results reported in other tokamaks. There is the potential for some of this missing ELM energy to be radiated away. Bolometric measurements on JET[60] and

ASDEX-Upgrade[61] indicate a fraction of the ELM energy is radiated away before being carried to the target, but the radiated power measurements do not have sufficient time resolution to distinguish between the initial ELM pulse, ≤200 μs, and later stages of the ELM cycle. In addition, modeling suggests that for ELMs in larger future devices, the higher power density ELMs will burn through the radiating lower ionization states of impurities before a significant fraction of the ELM energy can be radiated away.[62] The larger fraction of ELM energy missing from the divertor deposition of Fig. 19 is carried to the main chamber by radially propagating plasma filaments during the ELM instability as will be discussed in Sec. V.

The second factor for determining the divertor deposited ELM energy density is the split between the inboard and outboard divertors. Given the role of parallel transport in ELM deposition described above, divertor deposition would be expected to be larger at the outer divertor, nearer the ELM source at the LFS midplane. However, as indicated in Fig. 20 for JET,[56,63] most tokamaks have measured greater ELM energy deposition at the inboard divertor compared to the outboard. Similar measurements have been made in JT-60U,[59] DIII-D[58,64] and ASDEX-U.[65,66] In each device the inboard divertor energy deposition is 2–3 times the energy of the outboard divertor. These results are for the standard favorable toroidal field direction with $B \times \nabla B$ into the divertor. There is some evidence that this asymmetry is eliminated, or even reversed, for reversal of the toroidal field direction.[56,65] The practical implication of this observation is that the inboard divertor target becomes the more vulnerable to damage due to ELMs. An ameliorating aspect of this asymmetry is the steady-state heat flux between ELMs is peaked at the outboard divertor providing more headroom for the inboard side to accommodate the

ELM heat pulse. The causes for this deposition asymmetry are uncertain and it is thus difficult to predict with certainty if similar asymmetries will be observed in future larger tokamaks. While the dependence of the asymmetry on toroidal field direction suggests plasma drifts are involved, this topic remains an active area of research.

The final factor for predicting the divertor surface temperature rise due to an ELM is the divertor area over which the ELM is deposited, or the so-called "Wetted Area". A number of studies in different tokamaks have found the width of the ELM divertor heat flux to be broader than the steady-state heat flux between ELMs.[47,53,67] A more recent study with improved fast IR measurements on JET,[68] shown in Fig. 21, reveals that the ratio between ELM and steady-state divertor heat flux can vary widely. In this analysis the ELM wetted area is defined as the integral of the outboard divertor ELM energy deposition divided by the peak in the energy deposition profile. This definition is appropriate in that the ELM divertor profile is often very irregular, not fitting an exponential profile, and it is the peak that represents the risk for damage.

The variation in ELM size of Fig. 21 was produced by two parametric scans: plasma current and external gas puffing. The largest ELMs were obtained at higher plasma current, and its associated high pedestal pressure. Additional gas puffing to higher density and collisionality reduced the relative ELM size, with the smallest ELMs at low current and high normalized density. The scaling of this data suggests the ELM wetted area is correlated more strongly with absolute ELM size than relative ELM size produced by variation in collisionality. A DIII-D study[69] confirmed this correlation when smaller ELMs produced during ELM mitigation experiments with low collisionality pedestals resulted in smaller ELM wetted areas. Another important aspect of Fig. 21 is that the wetted area of the ELM scales differently than the steady-state inter-ELM profiles. Consistent with this scaling, multi machine studies[70-72] found the width of the inter-ELM heat flux to scale inversely midplane poloidal field, B_p^{-1}, or inversely with plasma current in a single device. This suggests that the physics setting the ELM deposition profile may be very different than that governing the inter-ELM hear flux profile. The scaling of the ELM wetted area represents a large uncertainty in projecting ELM heat fluxes to future tokamaks, and will be the subject of considerable future effort.

V. ELM transport to the main chamber

A fraction of the ELM energy also propagates radially into the SOL, eventually interacting with PFCs of the main chamber. This was first seen as a rapid rise in the far SOL electron density and temperature following the ELM onset with a Thomson scattering diagnostic[48] and later investigated with a wide range of diagnostics. Video imaging of ELM dynamics has revealed the ELM far SOL effects are due to radial propagation of filamentary structures.[32,73-75] An example of such filamentary structure is shown in Fig. 22. The filamentary structures are initially parallel to the magnetic field, and though their structure is more complex than a single mode, the average spacing between filaments is consistent with intermediate toroidal mode numbers of $5 \le n \le 15$. Linear stability analysis typically finds the most unstable mode to be of similar mode number to that of the observed filaments.[32,33]

Many observed characteristics of ELM filament propagation can be described by a model of electrostatic radial propagation and decay due to sheath limited parallel transport.[76] Langmuir probes inserted into the SOL provide the clearest indication of electrostatic propagation. A probe will typically measure multiple peaks with complex structure during a single ELM event as shown in Fig. 23.[77] The filament size is up to a couple of centimeters perpendicular to the magnetic field, similar to the pedestal width. Probes also measure an electric field in the filaments consistent with a radial $E \times B$ velocity of up to 1 km/s.[77-80] This inferred radial velocity has been confirmed with more direct measurements including video image analysis,[74] time delay measurements from the ELM onset[36,77] and fast microwave reflectometry measurements of density profiles.[43] The filaments also carry toroidal momentum as they emerge from the pedestal region, consistent with CER measurements of a flattening of the pedestal rotation profile described in Sec. III.[37] The toroidal rotation of the filaments rapidly damps after separation from the core plasma.[79,81] The ELM filaments remained aligned to the magnetic field as they propagate radially, adjusting their pitch in the same manner as the background field.[74] The velocity of the filaments is also correlated with size, with largest filaments having the largest radial velocity of 1 km/s, or more. This is consistent with the view of the filaments as interchange driven events, similar to that of L-mode “blobby” transport.[82] In fact the smallest ELM filaments become indistinguishable from the intermittent transport events in the SOL of L-mode plasmas.[80,83]

Parallel transport draining the ELM filaments as they propagate radially has been directly observed in spiral heat flux patterns on the divertor target,[33,84,85] such as that shown in Fig. 24.[85] This pattern is consistent with magnetic field line mapping of a plasma source at the outboard midplane that propagates radially. The associated magnetic field lines crossed by the radially propagating source trace out the same spiral pattern onto the divertor target as the heat flux pattern. The toroidal spacing of the spirals can be interpreted as an effective toroidal mode number that is again found consistent with the moderate mode numbers, n = 1020, from linear stability analysis.[33,85] The appearance of the multiple heat flux spirals is not simultaneous, but consistent with the random separation of the filaments from the core plasma over the course of a single ELM. The parallel heat flux lost from the filaments as they propagate leads to their decay, most quickly in electron temperature, as shown in Fig. 25. The losses are dominated by the faster electron conduction compared to slower losses of density and ion temperature, both of which occur on the timescale of thermal ion transit from the midplane to the divertor.

Measurements of ion energies with a Retarding Field Analyzer (RFA) at JET indicate the ion temperature within the ELM filament remains up to half of the pedestal ion temperature by the time the filament intercepts the main chamber limiter.[86] The ELM filament radial decay has also been measured on ASDEX-Upgrade with insertable Langmuir probes.[87] The radial decay length of heat flux inferred from the probes was consistent with the divertor ELM heat flux width measured by an IR camera. This correlation suggests the processes of the ELM filament model governing radial propagation and decay of the ELM filaments is similar to the processes controlling the divertor ELM heat flux profiles,[88] described previously in Sec. IV. However, the size, number and temperature of the filaments when they detach from the core plasma indicates they carry only about 10% of the total energy lost at an ELM.[79,89,90] Determining the exact relationship between ELM filament behavior and ELM divertor heat flux awaits further theoretical, simulation and experimental progress.

While the ELM filament deposition onto the main chamber wall represents a small fraction of the total ELM energy, this interaction does have important implications. Because of the high ion temperature remaining within the filaments, they present a significant risk of sputtering in future larger devices such as ITER where high pedestal temperatures of several keV are expected.[56] The ELM filaments can also account for a majority of the main chamber particle flux during H-mode.[91-93] This flux must be considered in the overall boundary plasma issues such as PFC erosion, migration and density control.

VI. ELM transport simulation

The experimental measurements of ELM heat flux described in the previous sections provide some expectations for ELM characteristics in future tokamaks, but a more complete physics basis is needed to provide confidence in extrapolating these results to much larger devices. While linear MHD stability analysis successfully predicts the pedestal conditions and mode structure involved at ELM onset, as described in Sec. II, prediction of energy and particle transport, as well as surface heat flux, requires additional physics. Boundary plasma fluid models have been used to assess ELM energy and particle transport,[94] but they typically rely on an ad-hoc increase in radial transport coefficients for a prescribed ELM duration. To fully simulate the ELM instability in a future tokamak the nonlinear MHD evolution, as well as the resulting transport, must be accounted for. This is a very challenging task due to the wide spatiotemporal scales and number of physics processes involved. The important spatial scales range from device size down to at least the ion gyro-radius with the time scale ranging from ion parallel transports processes down to Alfvèn times of MHD evolution and electron parallel transit times. The physical processes to be described include, MHD stability and nonlinear evolution, magnetic reconnection, turbulent transport, kinetic effects of low collisionality parallel transport, and plasma-material interactions. While a complete model is not yet available for full ELM simulation, recent efforts are highlighting the important physical processes involved and guiding the path forward for further progress.

Theoretical considerations of the ELM nonlinear MHD evolution describe explosive growth of the instability due to a non-linear weakening of the magnetic field line bending restoring force.[95] This theory predicts the ballooning instability to eject a flux tube from the high pressure pedestal region into the lower pressure edge. The ejected flux tubes narrow and twist to pass through overlying field lines, while maintaining their magnetic connection to the core plasma. To confirm this basic picture of the early stage of ELM evolution, a simulation with realistic experimental conditions was carried out with the 3D reduced Braginskii BOUT code[96] modified to include the equilibrium kink/peeling drive term[95] with a reduced toroidal domain ($n = 5,10,15,20\ldots160$). Initially a fast growing mode, $n = 20$, develops in the high gradient region, Fig. 26(a), with a spatial structure similar to that expected from linear stability analysis.[97] At a later stage as the mode grows and becomes nonlinear, one or more flux tubes burst radially crossing the separatrix, Fig. 26(b), resulting in a filamentary structure extended parallel to the magnetic field, but localized in the perpendicular direction. Another study with the M3D code[98] examined the implications of including the full spectrum of toroidal modes with very fine spatial resolution. While qualitatively the same expulsion of flux of magnetic flux tubes was observed as in earlier studies, the coupling of multiple unstable modes lead to a very complex stochastic magnetic field structure, as shown in Fig. 27. In addition, non-axisymmetric currents flowing in the SOL during an ELM may contribute to the formation of these complex magnetic structures.[99]

The complex magnetic structures of Fig. 27 highlight a challenge with advancing ELM simulation past the early nonlinear phase in order to describe the resulting energy and particle transport. At typical H-mode pedestal conditions, with a density of several 10^{19} m^{-3} and T_e up to 1 keV and higher, the low resistivity results in a current diffusion time much longer than the ELM growth rates or evolution time scale. This results in fine scale magnetic structure, and associated current structures that evolve down to the finest practical grid resolution and even physical plausibility. Different techniques and physical suppositions have been employed to deal with this challenge. One approach, used with the JOREK code,[100-102] is to assume a higher resistivity than the experimental conditions in order to examine the effects of a more rapid magnetic reconnection. In the simulation of a JET ELM shown in Fig. 28 the JOREK code used a single fluid resistive MHD model with a single $n = 8$ toroidal mode and a resistivity a factor of 100 higher than implied by the experimental parameters. The simulation resulted in pronounced filamentary structures of density temperature and current. The current filaments produce an ergodized edge magnetic structure as shown in Fig. 28. The ergodized edge allows parallel transport to carry heat flux from the pedestal to the divertor target reproducing a number of experimental observations, including the fraction of energy loss and the time duration of the ELM instability. The divertor heat flux pattern resulting from the magnetic field ergodization and homoclinic tangles is also similar to measurements, being wider than the inter-ELM heat flux, with spiral patterns similar to Fig. 24. In addition the heat flux pattern becomes broader with larger ELMs, again replicating experimental trends. These results suggest that if current diffusion and magnetic reconnection is faster than classical expectation, then parallel transport from the pedestal to the divertor target could account for much of experimental observations.

Additional physics to be included in ELM simulation is that of finite Lamor radius effects to more accurately capture the evolution of ballooning turbulence during the ELM. The BOUT++ code[103] employs a six-field two fluid model to describe these effects in realistic X-point geometry. The fine scale current structures that typically develop are dealt with by the supposition of a hyper-resistivity term that quickly diffuses current over the short spatial scales of electron turbulence, while leaving current diffusion over the broader pedestal profile at the classical resistivity level. BOUT++ simulations[104] indicate significant radial transport due to edge ergodization and resulting parallel transport, but the simulation also exhibited significant radial $E \times B$ flux from the ballooning mode turbulence. In fact, recent results[105,106] show that $E \times B$ radial flux can be the dominant channel for ion transport and can be similar or greater than parallel transport for electron heat transport.

The results summarized above highlight several areas where advances in simulation are needed for accurate prediction of ELM transport. The different treatments of resistivity point out the importance of understanding the level of magnetic reconnection resulting from an anomalous current diffusion above that given by classical resistivity. Faster current diffusion over a larger region of the pedestal leads to faster magnetic reconnection and larger radial flux due to parallel transport from the pedestal. Experimental verification of magnetic reconnection would greatly aid the validation ELM simulation models.

Another gap in the existing simulations is that they do not adequately describe the role of the H-mode transport barrier. The sheared rotation profile suppresses ballooning and drift wave turbulence that would otherwise result from the H-mode pedestal profiles. The ELM instability flattens the rotation profile and transport barrier thereby driving further radial transport. It is the re-establishment of the H-mode barrier that signals the end of the ELM. No existing models yet self-consistently simulate the formation of H-mode. Detailed ELM simulation awaits further progress on this front.

Finally it was noted in Sec. IV that kinetic effects play a significant role in parallel transport from the pedestal to the target. These effects must be accounted for the fluid simulations described above if an accurate assessment of ELM heat flux is to be made. Encouragingly it appears these kinetic effects may be adequately described in fluid models through the use of flux limits at low collisionality and appropriately chosen sheath boundary conditions.[107]

VII. Implications for future devices

The experimental observations and developing theory basis for ELM transport can be used to assess the risk for future large Tokamaks such as ITER and DEMO. Significant effort has been made evaluating the risk for ITER and the level of ELM mitigation that will be required to avoid damaging in-vessel components.[108-110] For carbon and ITER's candidate divertor target material of tungsten, Eq. (2) has been evaluated with the appropriate thermal characteristics for ablation and melting limits, respectively.[111] The "heat flux factor" (HFF) limit for both materials is similar at

$$\frac{\Delta W}{A\sqrt{\Delta t}} \le 50 \text{ MJ m}^{-2} \text{ s}^{-1/2} \quad , \tag{3}$$

where ΔW is the ELM energy deposited in the divertor over an area A in a time Δt.

For carbon, surface ablation sets the HFF limit. Decades of experience with carbon in tokamaks shows that, while indeed, exceeding this limit results in ablation of the surface, the effect is usually benign allowing subsequent successful plasma discharges. However with many ELMs expected in each discharge of future long-pulse burning plasma tokamaks, exceeding this limit on every ELM would result in an unacceptably short divertor lifetime.[112,113]

For tungsten, melting is the primary concern when exceeding the HFF limit. Tests in ELM pulse simulators[114-116] exhibit melting and removal of material for heat pulses greater than the 50 MJ m^{-2} $\text{s}^{-1/2}$ described in Eq. (3). Melting of the divertor target has also been shown to be detrimental to subsequent tokamak divertor operation.[117] For a large number of repetitions, ≥10,000, heat pulses a factor of 5 smaller than the HFF limit can still lead to degradation of the surface through grain growth, cracking and reduction of thermal conductivity.[115,118,119] However the long-term implications of these lower threshold effects are uncertain, and therefore not currently considered as limits for ITER design or operation.

The material thermal limitations, as well as the ELM divertor heat flux experimental observations of Sec. V have been taken into account to estimate the largest tolerable ELM size for ITER, as shown in Fig. 29, that does not result in melt/ablation of the divertor target.[108,110] The first assumption of this assessment is that the ELM heat flux rise time corresponds to the ion transit time from the pedestal to the divertor, $\tau_r \sim 300\ \mu s$, with a decay time ~2x longer. Thus only about 1/3 of the ELM energy contributes to driving the peak temperature. For the distribution of heat flux onto the divertor surface, the inboard target is assumed to accept 2/3 of the ELM energy lost from the core plasma, over an area 3-5 times greater than the inter-ELM heat flux area. The assumption for inter-ELM heat flux is based on recent multiple tokamak empirical scalings[70-72] which exhibit a heat flux width dependence inverse with the poloidal magnetic field, $\lambda_q \propto B_p^{-1}$, or inverse with the plasma current in a single device. With these assumptions and Eq. (3), the tolerable ELM size is displayed in Fig. 29 versus ITER's plasma current for an ELM heat flux width equal to the empirical inter-ELM width scaling and four times the inter-ELM scaling. This is compared to the natural ELM size expected in ITER at expected pedestal conditions[23,120] ($n_e \approx 1.0 \times 10^{19}\ \mathrm{m}^{-3}$ and $T_i = T_e \approx 3.5\ \mathrm{keV}$ for $Q = 10$ at 15 MA). The expected ITER ELM size clearly exceeds the tolerable ELM size, but the margin is a very strong function of plasma current. This dependence arises from the pedestal height dependence, $P_{ped} \propto I_p^2$, and a 20% fraction of the pedestal energy lost as suggested by the multi-tokamak scaling of Fig. 14.

Based on the scaling of Fig. 29, the ITER specification for tolerable ELMs calls for a reduction in natural ELM size of at least a factor of 20 to avoid divertor melting/ablation. The large conservative factor results from the observation that ELM width tends to narrow towards the inter-ELM width for small relative ELM size,[68,69] negating much of the benefit of small relative ELM size. Prospects for meeting the ITER requirements are described in Sec. VIII. However, this stringent requirement rests largely on an uncertain ELM heat flux width estimate. The data of Fig. 21 suggests different physics controls the width of the inter-ELM versus ELM heat flux. In addition there is no established physics basis for ELM heat flux width to add confidence in prediction of the above estimates. Clearly this is an area in need of additional work and multi-machine comparisons.

Risks to ITER's main chamber PFCs due to ELMs have also been assessed.[109] Main chamber components generally have less heat flux capacity in their design than the divertor target, and are thus more susceptible to damage due to transients. This is particularly true for ITER with the lower melting point of its beryllium main chamber components. However, the peak ELM heat flux occurs on the tungsten divertor and decays sufficiently quickly outside of this region that ELMs should not produce melting of the beryllium components. This estimate takes into consideration the narrowing of the ELM heat flux width with smaller relative ELM size, and the lower melting limit for ITER's beryllium main chamber wall. Another concern is the time-averaged heat flux to these components. As ELM filaments carry radially roughly 10% of the ELM energy, the upper secondary X-point in ITER where the heat flux can be concentrated may be of concern. Additional experimental analysis and design of high heat flux capacity panels for the secondary divertor are under consideration.

For future tokamaks beyond ITER, such as DEMO, the ELM heat flux is of even greater concern. This arises simply due to the higher power densities and greater plasma stored energy compared to machine size that are envisioned for these devices.[121-124] In addition these devices are expected to have high-Z metal main chamber walls that will be susceptible to erosion due to high T_i in the ELM filaments. This will likely produce unacceptable erosion and contamination of the core plasma for significant ELMs. For these reasons, ELM mitigation and control will almost certainly be required for reactor scale tokamaks. Plans and prospects for ELM control are briefly summarized in the next section.

VIII. ELM mitigation and control

ELM mitigation and control is a very active area of current fusion research, that has been summarized in several recent reports.[108,125-127] Because of the wide ranging effort and plethora of potential techniques, only a brief summary will be presented here, with an emphasis on how the present understanding of ELM physics presented in the previous sections is guiding current efforts.

The general approach to ELM control is to provide additional energy transport through the pedestal to avoid reaching the ELM MHD stability limit and enough additional particle transport to make up for the suppressed ELM and avoid impurity accumulation in the core plasma. One option for additional transport is through an intrinsic mode within the pedestal. Examples include small amplitude ELM-like bursts involving only a small part of the pedestal profile, and continuous modes providing transport through the pedestal. Another approach is to actively trigger an instability over part of the pedestal profile before it reaches the larger ELM instability. Finally additional transport through the pedestal may be obtained through external means such as the application of 3D magnetic fields. A brief summary of each of these approaches is given below.

A. Intrinsic ELM-free regimes

A number of operational regimes have been identified in existing devices with the high performance of H-mode, but without the large amplitude ELMs described above.[128,129] These regimes have a variety of names, including Type II, Type III, Type IV, Type V, EDA, I-mode, Grassy and QH-mode due to the specific characteristics associated with obtaining them in each device. Most of these modes are not thought to be applicable to future burning plasmas because of their specific operational requirements, usually either a high collisionality pedestal, or degraded pedestal pressure. Following is a brief description of each of these modes with some characteristics that make them unique.

Type II ELMs:[25,130-132] These ELMs are observed at high shaping, near double-null, and high collisionality, $\upsilon_e^* \sim 1$. They are marked by a turbulent edge recycling signal.

Type III ELMs:[25,131,133] A high density/collisionality regime marked by high frequency, small amplitude ELMs. They exist for power crossing the separatrix near the H-L back transition. They also exhibit low pedestal pressure, ≤70% of the large amplitude ELM pedestal limit.

Type IV ELMs:[134] A low collisionality regime, but at low input power near the L-H transition. Also marked by low pedestal pressure.

Type V ELMs:[135,136] An operational regime observed in the NSTX tokamak.

EDA[137,138] and HRS:[139] Similar high density and collisionality regimes observed in Alcator C-mod and JFT-2M respectively. A continuous mode observed in the pedestal provides additional particle transport.

Wall conditioning: Wall conditions have a long known effect on ELM characteristics, presumable through recylcing and fueling of the pedestal density profile. This is particularly true for lithium conditioning with application through evaporation or direct injection. Lithium conditioning has succeeded in NSTX[140-142] and EAST[143-145] in achieving significant reduction in ELM size, or even complete ELM suppression, through reducing edge recycling and modification of the pedestal density and pressure profile in a manner favorable for edge stability. Studies to determine how changes in edge fueling affect pedestal profiles and ELM stability are underway.

I-mode:[146,147] An enhanced confinement regime with a temperature pedestal, but no density pedestal. Enhanced density transport through pedestal allow for regime to be steady-state. Issues for application to burning plasmas include access conditions and attainable pedestal pressure for high global confinement.

QH-mode:[148] bears further examination due to its potential application to burning plasmas and the related ELM physics previously described in this review. The QH-mode, shown in Fig. 30, has been extensively studied in DIII-D, but also observed in ASDEX-Upgrade,[149,150] JET[150] and JT-60U.[151,152] An edge harmonic oscillation (EHO) active in the pedestal provides additional energy and particle transport to enable steady operation in this H-mode regime without ELMs. The EHO is found to be accessible along the kink/peeling boundary of ELM stability, as shown in Fig. 31, and modeled to be destabilized by rotational shear.[153,154] This mode is thought to saturate nonlinearly as the rotational shear driving the mode is damped at larger amplitude by the nearby conducting wall. This is in contrast to the peeling mode where the current driving the mode is maintained for growing amplitude by its own inductance. This regime is attractive for future burning plasmas because it is accessible at low pedestal collisionality with strong shaping and can achieve high pedestal pressure similar to the ELMing regime at similar parameters. Recent results have demonstrated that QH-mode can be maintained at higher normalized density, $n/n_{\mathrm{GW}} \sim 0.75$, relevant for divertor heat flux control. While burning plasma tokamaks will likely have low input torque, QH-mode was first obtained with strong neutral beam injection (NBI) heating counter to the plasma current direction where rotational shear in the pedestal is strongly driven. More recently QH-mode has been obtained with a more relevant low NBI torque by rotation driven from neoclassical toroidal viscosity (NTV) of applied 3D fields.[148] Further work is needed to provide a physics-based scaling of the rotational shear required to achieve the EHO and the input torque needed to achieve that shear.

B. ELM triggering

ELM control may also be obtained by triggering frequent smaller ELMs. The idea is to provide additional transport by frequently triggering an instability over a small portion of the pedestal before the larger ELM engulfs the entire pedestal. This is also motivated by the observation that ELM amplitude decreases with increasing ELM frequency,[67] providing a roughly fixed fraction, ~20%, of energy transport across the separatrix. Several techniques have been used to trigger frequent ELMs, including, pellet injection,[155-157] supersonic molecular beam injection (SMBI),[158-161] jogs to the plasma vertical position,[162-165] and oscillating applied magnetic fields.[166,167]

Pellet ELM pacing is a baseline ELM control option for ITER,[108] and highlights the important physics of triggered ELMs. The concept behind pellet pacing is to launch a fuel pellet with size and speed such that most of its density is deposited in the steep pressure gradient region of the pedestal. A localized region of high pressure is created when parallel electron transport carries heat to the cold pellet cloud faster than the high ion density can spread along the flux tube. If this localized pressure hill exceeds the MHD stability limit then an ELM can occur over a small region of the pedestal. Small frequent pellet injection on ASDEX-Upgrade demonstrated a factor of 3 increase in ELM frequency and similar reduction in ELM amplitude,[155,168] as shown in Fig. 32. This was accomplished while maintaining a robust pedestal pressure and good H-mode confinement. In DIII-D pellet pacing has recently demonstrated a factor of 12 increase in

ELM frequency with similar reduction in ELM energy for ITER similar discharges.[157] Other recent results in ASDEX-Upgrade and JET highlight some potential limitations to the obtainable ELM frequency increase while maintaining a robust pedestal.[156] Successful modeling of the DIII-D results for pellet deposition, local increase in pressure and resulting ELM instability with the JOREK code lends confidence in this overall approach ELM control.[169] Further work is still required to determine the minimum pellet size that is capable of triggering an ELM in order to limit the total particle throughput for the particle exhaust system. Pellet pacing should also demonstrate the compatibility of a robust pedestal with ITER's required factor of 20 increase in ELM frequency and reduction in ELM energy.

C. Applied resonant magnetic perturbations

The other ELM control system in ITER's baseline design is the use of resonant magnetic perturbations (RMPs) for ELM mitigation and suppression.[108,170] This concept is based upon applying non-axisymmetric magnetic fields to add additional transport through pedestal to maintain profiles below the ELM instability. This approach has demonstrated ELM suppression in DIII-D[171-175] as shown in Fig. 33. In this example, after the RMP coils are energized the pedestal density and pressure are subsequently reduced, resulting in a suppression of ELMs. Though a modest reduction in pedestal pressure occurs, the H-mode is maintained with good confinement. The constant density and radiated power levels indicate no increase in core plasma density and impurity confinement due to the suppression of ELMs. ELM mitigation and/or control with 3D fields has also been demonstrated in JET,[176,177] KSTAR,[160,161,178] MAST,[179-181] NSTX[166] and in ASDEX-Upgrade.[182-184]

A number of physics issues must still be resolved before RMP ELM control can be scaled with confidence from current experiments to future devices. The first is the plasma response to the applied fields. The tokamak plasma can screen out these fields due to plasma rotation and/or amplify the fields on resonant surfaces. Recent theory and modeling comparisons to experimental measurements suggest significant modification to the vacuum field approximation should be expected for H-mode experimental conditions.[185-188] Also the underlying physics of the additional transport with 3D fields must be validated in order to scale the applied magnetic field specifications to future devices with confidence. One potential mechanism is resonant magnetic islands form at the top of the pedestal due to RMP application, and limit expansion of the pedestal width to below that of the ELM stability limit.[154,189] Another important aspect is the additional density and impurity transport through the pedestal provided by the 3D fields, while maintaining a thermal transport barrier. Various mechanisms that may be responsible for the additional transport include, magnetic flutter transport,[190,191] and turbulent transport due to reduction of the $E{\times}B$ transport barrier.[174,192,193]

The operational constraints of RMP ELM control in future burning plasmas such as ITER must also be addressed. RMP ELM suppression has been successful in current devices at ITER's expected pedestal collisionality,[171,178] but can be lost at high normalized density ($n_e/n_{GW} \sim 1$) when collisionality is high. A physical model of RMP ELM suppression is needed to determine if pedestal collisionality alone is responsible for this dependence or whether some other aspect of high-normalized density operation on ITER will interfere with RMP ELM control. ITER's high-density operation will also require central fueling with pellets. RMP ELM suppression must also be shown to be compatible pellet fueling and maintain ELM suppression through pellet injection. Finally the low input torque and resulting low toroidal rotation of future burning plasma tokamaks makes them susceptible to locked modes. The compatibility of RMP field application at low torque and low toroidal rotation with the avoidance of locked modes must be understood and demonstrated.

A number of prospects for ELM heat flux mitigation and control in future burning plasma tokamaks have now been demonstrated in existing tokamaks, as summarized above. However, projection of the applicability of each of these techniques to future tokamaks will require further development of the underlying physics of the control mechanisms. These techniques have shown adequate reduction in relative ELM size and applicability at low pedestal collisionality. Other constraints of burning plasmas including high normalized density ($n/n_{GW} \sim 1$), low input torque, divertor heat flux control and limited particle pumping throughput, have yet to be fully addressed. Because these conditions cannot be simultaneously met in existing devices, such as low pedestal collisionality and high normalized density, confidence in projection of ELM control performance to burning plasma tokamaks requires a well established physics basis. The development of a physics basis for each of these techniques should be a priority moving forward.

IX. Summary

The wide range of results presented in this review has demonstrated great progress in the understanding of the ELM instability. This understanding has made possible the exploitation and optimization of the H-mode operational regime, as well as highlighting areas of concern for future work. The development of computational tools to accurately calculate the ELM MHD stability limit to peeling and ballooning modes, coupled with advances in pedestal transport physics,[23] now allows for prediction and optimization of pedestal parameters in future devices with confidence. As the pedestal pressure is such an important factor in determining global plasma performance, these tools represent a key resource for the overall optimization of the tokamak concept, for features including shape, size and magnetic field strength.

While ELMs provide additional particle transport through the pedestal to allow H-mode steady-state operation, the resulting heat flux transients represent a risk to the internal components of future devices. This risk can be evaluated by projection of the ELM energy deposited onto material surfaces and the time for that deposition. The ELM energy lost from the core plasma is well correlated across devices when properly normalized for pedestal pressure. The processes of parallel transport due to magnetic reconstruction, and turbulent transport due to the collapse of the H-mode transport barrier have been identified as possible channels for the ELM lost energy, but simulation is not yet able to quantify the relative roles of these processes. The time dependence of the ELM energy deposition onto surfaces has been correlated across devices with the thermal transit time from the pedestal to the divertor in the SOL. The observed time dependence is reproduced by theory and simulation. The profile of ELM energy deposition, however, is much less well characterized by experiment, nor understood by theory. The divergent scalings of ELM heat flux width and inter-ELM heat flux width suggest that different processes are important for each. This is clearly an area where experimental comparisons across devices and theoretical work are needed.

The assessments of experimental results indicate that mitigation or even complete suppression of ELMs will be needed to protect PFCs in future burning plasma tokamaks. Encouraging results have been obtained in existing devices with leading candidates being intrinsic modes such as QH-mode, ELM pacing with pellets and application of 3D resonant magnetic fields. Intrinsic modes of operation have an inherent appeal in that they do not require specialized hardware that may be difficult, or even impossible, to implement within the constraints of power plant scale tokamaks. QH-mode is a leading candidate due to its access at low pedestal collisionality and other operational parameters. However, a physics basis, or at a minimum a rigorous empirical scaling, must be developed for QH-mode, or any other potential intrinsic regime, in order to project its access and performance to future burning plasmas. ELM-pacing with pellets is a baseline ELM control system for ITER and is attractive because the pellet injection system is separate and removed from tokamak vessel and associated hardware. However, the required performance is still to be established in terms of reducing ELM energy to the required level, maintaining pedestal pressure, and the required particle throughput. The other technique in ITER's baseline ELM control plan, the application of 3D resonant magnetic fields, has the advantage that it has demonstrated complete ELM suppression in several existing devices, and at pedestal collisionalities expected in burning plasmas. As with the other ELM control schemes, this technique must be shown to be compatible with the operational constraints of a burning plasma including maintaining a high pedestal pressure, compatibility with divertor heat flux control and susceptibility to locked modes due to low input torque. A model, preferably physics-based, is needed to address these concerns and to optimize the design and operation of a 3D coil set.

ELM research has resulted in progress across a wide range of fusion science, including nonlinear MHD evolution, turbulent plasma transport, open field line transport, plasma kinetic effects, and plasma-material interactions. Progress on this diverse set of topics has resulted in new understanding of fundamental plasma physics, optimization of the tokamak concept, and promising prospects for ELM control in future burning plasma tokamaks. Continued focused work in this area is needed to fully realize the prospects for fusion energy development.

Acknowledgments

This work was supported by the US Department of Energy under DE-FC02-04ER54698. The author gratefully acknowledges the members of the International Tokamak Physics Activity (ITPA) Pedestal and Edge Physics and Scrape Off Layer and Divertor topical groups. These two groups have contributed greatly to progress reviewed here. The author would also like to thank the many individuals who contributed to assembling this review, particularly, A. Kirk, T.H. Osborne, R.A. Pitts, P.B. Snyder, and X.Q. Xu. DIII-D data shown in this paper can be obtained in digital format by following the links at https://fusion.gat.com/global/D3D_DMP.

References

[1]F. Wagner, G. Becker, K. Behringer, D. Campbell, A. Eberhagen, W. Engelhardt, G. Fussmaann, O. Gehre, J. Gernhardt, G. v. Gierke, G. Haas, M. Huang, F. Karger, M. Keilhacker, O. Klüber, M. Kornherr, K. Lackner, G. Lisitano, G. G. Lister, H, M. Mayer, D. Meisel, E. R. Müller, H. Murmann, H. Niedermeyer, W. Poschenrieder, H. Rapp, H. Röhr, F. Schneider, G. Siller, E. Speth, A. Stäbler, K. H. Steuer, G. Venus, O. Vollmer, and Z. Yü, Phys. Rev. Lett. **49**, 1408 (1982).

[2]M. Keilhacker, G. Becker, K. Bernhardi, A. Eberhagen, M. ElShaer, G. FuBmann, O. Gehre, J. Gernhardt, G. von Gierke, E. Glock, G. Haas, F. Karger, S. Kissel, O. Klüber, K. Kornherr, K. Lackner, G. Lisitano, G. G. Lister, J. Massig, H. M. Mayer, K. McCormick, D. Meisel, E. Meservey, E. R. Müller, H. Murmann, H. Niedermeyer, W. Poschenrieder, H. Rapp, B. Richter, H. Röhr, F. Ryter, F. Schneider, S. Siller, P. Smeulders, F. Soldner, E. Speth, A. Stäbler, K. Steinmetz, K.-H. Steuer, Z. Szymanski, G. Venus, O. Vollmer, and F. Wagner, Plasma Phys. Control. Fusion **26**, 49 (1984).

[3]T. Pütterich, R. Dux, M. A. Janzer, R. M. McDermott, and ASDEX Upgrade Team, J. Nucl. Mater. **415**, S334 (2011).

[4]C. C. Petty, M. E. Austin, C. T. Holcomb, R. J. Jayakumar, R. J. La Haye, T. C. Luce, M. A. Makowski, P. A. Politzer, and M. R. Wade, Phys. Rev. Lett. **102**, 045005 (2009).

[5]T. C. Luce, M. R. Wade, J. R. Ferron, P. A. Politzer, A. W. Hyatt, A. C. C. Sips, and M. Murakami, Phys. Plasmas **11**, 2627 (2004).

[6]ASDEX Team, Nucl. Fusion **29**, 1959 (1989).

[7]K.H. Burrell, Phys. Plasmas **4**, 1499 (1997).

[8]R. J. Groebner, Phys. Fluids B: Plasma Physics **5**, 2343 (1993).

[9]W. Mandl, K. H. Burrell, R. J. Groebner, J. Kim, R. P. Seraydarian, M. R. Wade, and J. T. Scoville, Nucl. Fusion **35**, 347 (1995).

[10]S. P. Hirshman, Phys. Fluids **31**, 3150 (1988).

[11]O. Sauter, C. Angioni, and Y. R. Lin-Liu, Phys. Plasmas **6**, 2834 (1999).

[12]S. Koh, C. S. Chang, S. Ku, J. E. Menard, and H. Weitzner, Phys. Plasmas **19**, 072505 (2012).

[13]E. A. Belli and J. Candy, Plasma Phys. Control. Fusion **50**, 095010 (2008).

[14]M. R. Wade, M. Murakami, and P. A. Politzer, Phys. Rev. Lett. **92**, 235005 (2004).

[15]D. M. Thomas, A. W. Leonard, R. J. Groebner, T. H. Osborne, T. A. Casper, P. B. Snyder, and L. L. Lao, Phys. Plasmas **12**, 056123 (2005).

[16]D. M. Thomas, A. W. Leonard, L. L. Lao, T. H. Osborne, H. W. Mueller, and D. F. Finkenthal, Phys. Rev. Lett. **93**, 065003 (2004).

[17]H. R. Wilson, P. B. Snyder, G. T. A. Huysmans, and R. L. Miller, Phys. Plasmas **9**, 1277 (2002).

[18]P. B. Snyder, H. R. Wilson, J. R. Ferron, L. L. Lao, A. W. Leonard, T. H. Osborne, A. D. Turnbull, D. Mossessian, M. Murakami, and X. Q. Xu, Phys. Plasmas **9**, 2037 (2002).

[19]P. B. Snyder, H. R. Wilson, J. R. Ferron, and L. L. Lao, Nucl. Fusion **44**, 320 (2004).

[20]N. Aiba, S. Tokuda, T. Fujita, T. Ozeki, and M. S. Chu, Plasma and Fusion Research **2**, 010 (2007).

[21]S. Yu. Medvedev, A. A. Martynov, Y. R. Martin, O. Sauter, and L. Villard, Plasma Phys. Control. Fusion **48**, 927 (2006).

[22]P. B. Snyder, N. Aiba, M. Beurskens, R. J. Groebner, L. D. Horton, A. E. Hubbard, J. W. Hughes, G. T. A. Huysmans, Y. Kamada, A. Kirk, C. Konz, A. W. Leonard, J. Lönnroth, C. F. Maggi, R. Maingi, T. H. Osborne, N. Oyama, A. Pankin, S. Saarelma, G. Saibene, J. L. Terry, H. Urano, and H. R. Wilson, Nucl. Fusion **49**, 085035 (2009).

[23]P. B. Snyder, R. J. Groebner, J. W. Hughes, T. H. Osborne, M. Beurskens, A. W. Leonard, H. R. Wilson, and X. Q. Xu, Nucl. Fusion **51**, 103016 (2011).

[24]P. B. Snyder, H. R. Wilson, T. H. Osborne, and A. W. Leonard, Plasma Phys. Control. Fusion **46**, A131 (2004).

[25]E. J. Doyle, R. J. Groebner, K. H. Burrell, and P. Gohil, Phys. Fluids B: Plasma Physics **3**, 2300 (1991).

[26]A. Loarte, G. Saibene, and R. Sartori, Plasma Phys. Control. Fusion **45**, 1549 (2003).

[27]C. P. Perez, H. R. Koslowski, G. T. A. Huysmans, T. C. Hender, P. Smeulders, B. Alper, E. de la Luna, R. J. Hastie, L. Meneses, M. F. F. Nave, V. Parail, M. Zerbini and JET-EFDA Contributors, Nucl. Fusion **44**, 609 (2004).

[28]J. L. Terry, I. Cziegler, A. E. Hubbard, J. A. Snipes, J. W. Hughes, M. J. Greenwald, B. LaBombard, Y. Lin, P. Phillips, and S. Wukitch, J. Nucl. Mater. **363-365**, 994 (2007).

[29]E. J. Strait, T. A. Casper, M. S. Chu, and J. R. Ferron, Phys. Plasmas **4**, 1783 (1997).

[30]T. H. Osborne, A. W. Leonard, M. A. Mahdavi, M. Chu, M. E. Fenstermacher, R. La Haye, G. McKee, T. W. Petrie, E. Doyle, G. Staebler, M. R. Wade, and DIII-D Team, Phys. Plasmas **8**, 2017 (2001).

[31]G. S. Yun, W. Lee, M. J. Choi, J. Lee, H. K. Park, B. Tobias, C. W. Domier, N. C.

Luhmann, A. J. H. Donné, J. H. Lee, and the KSTAR Team, Phys. Rev. Lett. **107**, 045004 (2011).

[32]M. E. Fenstermacher, T. H. Osborne, A. W. Leonard, P. B. Snyder, D. M. Thomas, J. A. Boedo, T. A. Casper, R. J. Groebner, M. Groth, M. A. H. Kempenaars, A. Loarte, G. R. McKee, W. M. Meyer, G. Saibene, M. A. Van Zeeland, X. Q. Xu, L. Zeng, and the DIII-D Team, Nucl. Fusion **45**, 1493 (2005).

[33]S. J. P. Pamela, G. T. A. Huijsmans, A. Kirk, I. T. Chapman, J. R. Harrison, R. Scannell, A. J. Thornton, M. Becoulet, F. Orain, and the MAST Team, Plasma Phys. Control. Fusion **55**, 095001 (2013).

[34]A. W. Leonard, R. J. Groebner, M. A. Mahdavi, T. H. Osborne, M. E. Fenstermacher, C. J. Lasnier, and T. W. Petrie, Plasma Phys. Control. Fusion **44**, 945 (2002).

[35]A. Loarte, M. Becoulet, G. Saibene, R. Sartori, D. J. Campbell, T. Eich, A. Herrmann, M. Laux, W. Suttrop, B. Alper, P. J. Lomas, G. Matthews, S. Jachmich, J. Ongena, P. Innocente, and E. J. W. Collaborators, Plasma Phys. Control. Fusion **44**, 1815 (2002).

[36]A. Kirk, H. R. Wilson, R. Akers, N. J. Conway, G. F. Counsell, S. C. Cowley, J. Dowling, B. Dudson, A. Field, F. Lott, B. Lloyd, R. Martin, H. Meyer, M. Price, D. Taylor, M. Walsh, and the MAST Team, Plasma Phys. Control. Fusion **47**, 315 (2005).

[37]M. R. Wade, K. H. Burrell, J. T. Hogan, A. W. Leonard, T. H. Osborne, P. B. Snyder, and D. Coster, Phys. Plasmas **12**, 056120 (2005).

[38]A. Loarte, G. Saibene, R. Sartori, T. Eich, A. Kallenbach, W. Suttrop, M. Kempenaars, M. Beurskens, M. de Baar, J. Lönnroth, P. J. Lomas, G. Matthews, W. Fundamenski,

V. Parail, M. Becoulet, P. Monier-Garbet, E. de la Luna, B. Goncalves, C. Silva, Y. Corre, Contributors to the EFDA-JET Workprogramme, Phys. Plasmas **11**, 2668 (2004).

[39]N. Oyama, N. Asakura, A. V. Chankin, T. Oikawa, M. Sugihara, H. Takenaga, K. Itami, Y. Miura, Y. Kamada, K. Shinohara, and JT-60 Team, Nucl. Fusion **44**, 582 (2004).

[40]I. Nunes, G. D. Conway, A. Loarte, M. Manso, F. Serra, W. Suttrop, the CFN and ASDEX-U Teams, Nucl. Fusion **44**, 883 (2004).

[41]A. Kirk, G. F. Counsell, H. R. Wilson, and J.-W. Ahn, Plasma Phys. Control. Fusion **46**, 551 (2004).

[42]M. R.Wade, K. H. Burrell, A. W. Leonard, T. H. Osborne, and P. B. Snyder, Phys. Rev. Lett. **94**, 225001 (2005).

[43]L. Zeng, G. Wang, E. J. Doyle, T. L. Rhodes, W. A. Peebles, G. R. McKee, R. Fonck, K. H. Burrell, M. E. Fenstermacher, J. A. Boedo, and R. A. Moyer, Plasma Phys. Control. Fusion **46**, A121 (2004).

[44]A. V. Chankin, N. Asakura, T. Fukuda, A. Isayama, Y. Kamada, Y. Miura, N. Oyama, S. Takeji, and H. Takenaga, Nucl. Fusion **42**, 733 (2002).

[45]M. Groth, M. E. Fenstermacher, and J. A. Boedo, N. H. Brooks, D. S. Gray, C. J. Lasnier, A. W. Leonard, G. D. Porter, and J. G. Watkins, J. Nucl. Mater. **313-316**, 1071 (2003).

[46]T. W. Petrie, J. G. Watkins, L. L. Lao, and P. B. Snyder, Nucl. Fusion **43**, 910 (2003).

[47]A. W. Leonard, A. Herrmann, K. Itami, J. Lingertat, A. Loarte T. H. Osborne, W. Suttrop, the ITER Divertor Modeling and Database Expert Group, and the ITER Divertor Physics Expert Group, J. Nucl. Mater. **266-269**, 109 (1999).

[48]A. W. Leonard, T. H. Osborne, M. E. Fenstermacher, R. J. Groebner, M. Groth, C. J. Lasnier, M. A. Mahdavi, T. W. Petrie, P. B. Snyder, J. G. Watkins, and L. Zeng, Phys. Plasmas **10**, 1765 (2003).

[49]A. W. Leonard, R. J. Groebner, T. H. Osborne, and P. B. Snyder, Phys. Plasmas **15**, 056114 (2008).

[50]T. Eich, A. Herrmann, P. Andrew, A. Loarte, Contributors to the EFDA-JET Program, J. Nucl. Mater. **313-316**, 919 (2003).

[51]A. Herrmann, W. Junker, K. Günther, S. Borsch, M. Kaufmann, J. Neuhauser, G. Pautasso, Th. Richter, and R. Schneider, Plasma Phys. Control. Fusion **37**, 17 (1995).

[52]T. Eich, A. Herrmann, G. Pautasso, P. Andrew, N. Asakura, J. A. Boedo, Y. Corre, M. E. Fenstermacher, J. C. Fuchs, W. Fundamenski, G. Federici, E. Gauthier, B. Goncalves, O. Gruber, A. Kirk, A. W. Leonard, A. Loarte, G. F. Matthews, J. Neuhauser, R. A. Pitts, V. Riccardo, and C. Silva, J. Nucl. Mater. **337-339**, 669 (2005).

[53]A. Loarte, B. Lipschultz, A. S. Kukushkin, G. F. Matthews, P. C. Stangeby, N. Asakura, G. F. Counsell, G. Federici, A. Kallenbach, K. Krieger, A. Mahdavi, V. Philipps, D. Reiter, J. Roth, J. Strachan, D. Whyte, R. Doerner, T. Eich, W. Fundamenski, A. Herrmann, M. Fenstermacher, P. Ghendrih, M. Groth, A. Kirschner, S. Konoshima, B. LaBombard, P. Lang, A. W. Leonard, P. Monier-Garbet, R. Neu, H. Pacher, B. Pegourie, R. A. Pitts, S. Takamura, J. Terry, E. Tsitrone, and the ITPA Scrape-Off Layer and Divertor Physics Topical Group, Nucl. Fusion **47**, S203 (2007).

[54]A. Bergmann, Nucl. Fusion **42**, 1162 (2002).

[55]D. Tskhakaya, R. A. Pitts, W. Fundamenski, T. Eich, S. Kuhn, and the JET EFDA Contributors, J. Nucl. Mater. **390-391**, 335 (2009).

[56]R. A. Pitts, P. Andrew, G. Arnoux, T. Eich, W. Fundamenski, A. Huber, C. Silva, D. Tskhakaya, and the JET EFDA Contributors, Nucl. Fusion **47**, 1437 (2007).

[57]T. Takizuka and M. Hosokawa, Contributions to Plasma Physics **46**, 698 (2006).

[58]A. W. Leonard, W. Suttrop, T. H. Osborne, T. E. Evans, D. N. Hill, A. Herrmann, C. J. Lasnier, D. M. Thomas, J. G. Watkins, W. P. West, M. Weinich, and H. Zohm, J. Nucl. Mater. **241-243**, 628 (1997).

[59]K. Itami, N. Hosogane, N. Asakura, H. Kubo, S. Tsuji, and M. Shimada, J. Nucl. Mater. **220-222**, 203 (1995).

[60]R.A. Pitts, G. Arnoux, M. Beurskens, T. Eich, W. Fundamenski, A. Huber, A. Loarte, J. Marki, M.F. Stamp, P. Andrew, S. Brezinsek, H.G. Esser, B. Gulejova, S. Jachmich, A. Kreter, E. de la Luna, G.F. Matthews, V. Philipps, E. Solano, and J.-E. contributors, J. Nucl. Mater. 390-391, 755 (2009).

[61]J. C. Fuchs, T. Eich, A. Herrmann, K. F. Mast, and the ASDEX Upgrade Team, J. Nucl. Mater. **337-339**, 756 (2005).

[62]A. Loarte, J. Nucl. Mater. **241-243**, 118 (1997).

[63]T. Eich, A. Kallenbach, W. Fundamenski, A. Herrmann, V. Naulin, JET-EFDA Contributors, and the ASDEX-Upgrade Team, J. Nucl. Mater. **390-391**, 760 (2009).

[64]M. E. Fenstermacher, A. W. Leonard, P. B. Snyder, J. A. Boedo, N. H. Brooks, R. J. Colchin, D. S. Gray, R. J. Groebner, M. Groth, E. Hollmann, C. J. Lasnier, T. H. Osborne, T. W. Petrie, D. L. Rudakov, H. Takahashi, J. G. Watkins, L. Zeng, and the DIII-D Team, Plasma Phys. Control. Fusion **45**, 1597 (2003).

[65]T. Eich, A. Kallenbach, R. A. Pitts, S. Jachmich, J. C. Fuchs, A. Herrmann, and J. Neuhauser, ASDEX Upgrade Team and JET-EFDA Contributors, J. Nucl. Mater. **363-365**, 989 (2007).

[66] A. Herrmann, T. Eich, S. Jachmich, M. Laux, P. Andrew, A. Bergmann, A. Loarte, J. Neuhauser, ASDEX Upgrade Team, Contributors to EFDA-JET Work Programme, J. Nucl. Mater. **313-316**, 759 (2003).

[67]A. Herrmann, Plasma Phys. Control. Fusion **44**, 883 (2002).

[68]T. Eich, H. Thomsen, W. Fundamenski, G. Arnoux, S. Brezinsek, S. Devaux, A. Herrmann, S. Jachmich, J. Rapp, and JET-EFDA Contributors, J. Nucl. Mater. **415**, S856 (2011).

[69]M. W. Jakubowski, T. E. Evans, M. E. Fenstermacher, M. Groth, C. J. Lasnier, A. W. Leonard, O. Schmitz, J. G. Watkins, T. Eich, W. Fundamenski, R. A. Moyer, R. C. Wolf, L. B. Baylor, J. A. Boedo, K. H. Burrell, H. Frerichs, J. S. deGrassie, P. Gohil, I. Joseph, S. Mordijck, M. Lehnen, C. C. Petty, R. I. Pinsker, D. Reiter, T. L. Rhodes, U. Samm, M. J. Schaffer, P. B. Snyder, H. Stoschus, T. Osborne, B. Unterberg, E. Unterberg, and W. P. West, Nucl. Fusion **49**, 095013 (2009).

[70]T. Eich, B. Sieglin, A. Scarabosio, W. Fundamenski, R. J. Goldston, A. Herrmann, and the ASDEX Upgrade Team, Phys. Rev. Lett. **107**, 215001 (2011).

[71]M. A. Makowski, D. Elder, T. K. Gray, B. LaBombard, C. J. Lasnier, A. W. Leonard, R. Maingi, T. H. Osborne, P. C. Stangeby, J. L. Terry, and J. Watkins, Phys. Plasmas **19**, 056122 (2012).

[72]T. Eich, A. W. Leonard, R. A. Pitts, W. Fundamenski, R. J. Goldston, T. K. Gray, A. Herrmann, A. Kirk, A. Kallenbach, O. Kardaun, A. S. Kukushkin, B. LaBombard,

R. Maingi, M. A. Makowski, A. Scarabosio, B. Sieglin, J. Terry, A. Thornton, ASDEX Upgrade Team, JET EFDA Contributors, Nucl. Fusion **53**, 093031 (2013).

[73]A. Kirk, H. R. Wilson, G. F. Counsell, R. Akers, E. Arends, S. C. Cowley, J. Dowling, B. Lloyd, M. Price, M. Walsh, and MAST Team, Phys. Rev. Lett. **92**, 245002 (2004).

[74]A. Kirk, N. B. Ayed, G. Counsell, B. Dudson, T. Eich, A. Herrmann, B. Koch, R. Martin, A. Meakins, S. Saarelma, R. Scannell, S. Tallents, M. Walsh, H. R. Wilson, and the MAST Team, Plasma Phys. Control. Fusion **48**, B433 (2006).

[75]R. J. Maqueda, R. Maingi, and the NSTX Team, Phys. Plasmas **16**, 056117 (2009).

[76]W. Fundamenski, R. A. Pitts, and the JET-EFDA Contributors, Plasma Phys. Control. Fusion **48**, 109 (2005).

[77]C. Silva, B. Goncalves, C. Hidalgo, K. Erents, A. Loarte, G. Matthews, and M. Pedrosa, J. Nucl. Mater. **337-339**, 722 (2005).

[78]A. Kirk, T. Eich, A. Herrmann, H. W. Müller, L. D. Horton, G. F. Counsell, M. Price, V. Rohde, V. Bobkov, B. Kurzan, J. Neuhauser, H. Wilson, and the ASDEX Upgrade and MAST Teams, Plasma Phys. Control. Fusion **47**, 995 (2005).

[79]J. A. Boedo, D. L. Rudakov, E. Hollmann, D. S. Gray, K. H. Burrell, R. A. Moyer, G. R. McKee, R. Fonck, P. C. Stangeby, T. E. Evans, P. B. Snyder, A. W. Leonard, M. A. Mahdavi, M. J. Schaffer, W. P. West, M. E. Fenstermacher, M. Groth, S. L. Allen, C. Lasnier, G. D. Porter, N. S. Wolf, R. J. Colchin, L. Zeng, G. Wang, J. G. Watkins, T. Takahashi, and DIII-D Team, Phys. Plasmas **12**, 072516 (2005).

[80]B. Goncalves, C. Hidalgo, M. A. Pedrosa, C. Silva, R. Balbín, K. Erents, M. Hron, A. Loarte, and G. Matthews, Plasma Phys. Control. Fusion **45**, 1627 (2003).

[81]J. A. Boedo, D. L. Rudakov, E. M. Hollmann, R. A. Moyer, G. R. McKee, K. Burrell,

T. E. Evans, A. W. Leonard, W. P. West, M. E. Fenstermacher, M. Groth, S. L. Allen, L. Zeng, G. Wang, and J. G. Watkins, J. Nucl. Mater. **337-339**, 771 (2005).

[82]O. E. Garcia, N. H. Bian, and W. Fundamenski, Phys. Plasmas **13**, 082309 (2006).

[83]J. A. Boedo, D. L. Rudakov, R. A. Moyer, G. R. McKee, R. J. Colchin, M. J. Schaffer, P. G. Stangeby, W. P. West, S. L. Allen, T. E. Evans, R. J. Fonck, E. M. Hollmann, S. Krasheninnikov, A. W. Leonard, W. Nevins, M. A. Mahdavi, G. D. Porter, G. R. Tynan, D. G. Whyte, and X. Xu, Phys. Plasmas **10**, 1670 (2003).

[84]T. Eich, A. Herrmann, J. Neuhauser, and the ASDEX Upgrade Team, Phys. Rev. Lett. **91**, 195003 (2003).

[85]T. Eich, A. Herrmann, J. Neuhauser, R. Dux, J. C. Fuchs, S. Günter, L. D. Horton, A. Kallenbach, P. T. Lang, C. F. Maggi, M. Maraschek, V. Rohde, W. Schneider, and the ASDEX Upgrade Team, Plasma Phys. Control. Fusion **47**, 815 (2005).

[86]R. A. Pitts, W. Fundamenski, S. K. Erents, Y. Andrew, A. Loarte, C. Silva, and JET-EFDA Contributors, Nucl. Fusion **46**, 82 (2005).

[87]A. Herrmann, A. Kirk, A. Schmid, B. Koch, M. Laux, M. Maraschek, H. W. Mueller, J. Neuhauser, V. Rohde, M. Tsalas, and E. Wolfrum, J. Nucl. Mater. **363-365**, 528 (2007).

[88]W. Fundamenski and R. A. Pitts, J. Nucl. Mater. **363-365**, 319 (2007).

[89]A. Herrmann, T. Eich, V. Rohde, C. J. Fuchs, J. Neuhauser, and the ASDEX Upgrade Team, Plasma Phys. Control. Fusion **46**, 971 (2004).

[90]W. Fundamenski and W. Sailer, Plasma Phys. Control. Fusion **46**, 233 (2004).

[91]D. L. Rudakov, J. A. Boedo, R. A. Moyer, P. C. Stangeby, J. G. Watkins, D. G. Whyte, L. Zeng, N. H. Brooks, R. P. Doerner, T. E. Evans, M. E. Fenstermacher, M. Groth,

E. M. Hollmann, S. I. Krasheninnikov, C. J. Lasnier, A. W. Leonard, M. A. Mahdavi, G. R. McKee, A. G. McLean, A. Y. Pigarov, W. R. Wampler, G. Wang, W. P. West, and C. P. C. Wong, Nucl. Fusion **45**, 1589 (2005).

[92]D. L. Rudakov, J. A. Boedo, J. H. Yu, N. H. Brooks, M. E. Fenstermacher, M. Groth, E. M. Hollmann, C. J. Lasnier, A. G. McLean, R. A. Moyer, P. C. Stangeby, G. R. Tynan, W. R. Wampler, J. G. Watkins, W. P. West, C. P. C. Wong, R. J. Bastasz, D. Buchenaueqr, and J. Whaley, J. Nucl. Mater. **390-391**, 785 (2009).

[93]A. Herrmann, J. Neuhauser, V. Rohde, R. Dux, T. Eich, C. J. Fuchs, and M. Y. Ye, J. Nucl. Mater. **337-339**, 697 (2005).

[94]D. P. Coster, J. Nucl. Mater. **390-391**, 826 (2009).

[95]H. Wilson and S. Cowley, Phys. Rev. Lett. **92**, 175006 (2004).

[96]X. Q. Xu, R. H. Cohen, W. M. Nevins, G. D. Porter, M. E. Rensink, T. D. Rognlien, J. R. Myra, D. A. D'Ippolito, R. A. Moyer, P. B. Snyder, and T. N. Carlstrom, Nucl. Fusion **42**, 21 (2002).

[97]P. B. Snyder, H. R. Wilson, and X. Q. Xu, Phys. Plasmas **12**, 056115 (2005).

[98]L. E. Sugiyama and H. R. Strauss, Phys. Plasmas **17**, 062505 (2010).

[99]T. E. Evans, J. H. Yu, M. W. Jakubowski, O. Schmitz, J. G. Watkins, and R. A. Moyer, J. Nucl. Mater. **390-39**1, 789 (2009).

[100]G. T. A. Huysmans, S. Pamela, E. van der Plas, and P. Ramet, Plasma Phys. Control. Fusion **51**, 124012 (2009).

[101]G. T. A. Huijsmans and A. Loarte, Nucl. Fusion **53**, 123023 (2013).

[102]S. J. P. Pamela, G. T. A. Huysmans, M. N. A. Beurskens, S. Devaux, T. Eich, S. Benkadda, JET EFDA Contributors, Plasma Phys. Control. Fusion **53**, 054014

(2011).

[103]X. Q. Xu, B. Dudson, P. B. Snyder, M. V. Umansky, and H. Wilson, Phys. Rev. Lett. **105**, 175005 (2010).

[104]T. Y. Xia, X. Q. Xu, and P. W. Xi, Nucl. Fusion **53**, 073009 (2013).

[105]J. Peer, A. Kendl, and B. D. Scott, Plasma Phys. Control. Fusion **55**, 015002 (2012).

[106]T. Y. Xia, X. Q. Xu, and M. E. Fenstermacher, Bull. Am. Phys. Soc. **58**, 251 (2013).

[107]E. Havlickova, W. Fundamenski, D. Tskhakaya, G. Manfredi, and D. Moulton, Plasma Phys. Control. Fusion **54**, 045002 (2012).

[108]A. Loarte, G. Huijsmans, S. Futatani, L. R. Baylor, T. E. Evans, D. M. Orlov, O. Schmitz, M. Becoulet, P. Cahyna, Y. Gribov, A. Kavin, A. Sashala Naik, D. J. Campbell, T. Casper, E. Daly, H. Frerichs, A. Kischner, R. Laengner, S. Lisgo, R. A. Pitts, G. Saibene, and A. Wingen, Nucl. Fusion **54**, 033007 (2014)

[109]R. A. Pitts, S. Carpentier, F. Escourbiac, T. Hirai, V. Komarov, A. S. Kukushkin, S. Lisgo, A. Loarte, M. Merola, R. Mitteau, A. R. Raffray, M. Shimada, and P. C. Stangeby, J. Nucl. Mater. **415**, S957 (2011).

[110]R. A. Pitts, S. Carpentier, F. Escourbiac, T. Hirai, V. Komarov, S. Lisgo, A. S. Kukushkin, A. Loarte, M. Merola, A. S. Naik, R. Mitteau, M. Sugihara, B. Bazylev, and P. C. Stangeby, J. Nucl. Mater. **438**, S48 (2013).

[111]G. Pintsuk, J. Compan, T. Hirai, J. Linke, M. Rodig, and I. Uytdenhouwen, Proc. of 22nd IEEE/NPSS Symposium on Fusion Engineering, Albuquerque, NM, Vol. 1 (Institute of Electrical and Electronics Engineers, Piscataway, 2007).

[112]G. Federici, A. Loarte, and G. Strohmayer, Plasma Phys. Control. Fusion **45**, 1523 (2003).

[113]V. Philipps, J. Nucl. Mater. **415**, S2 (2011).

[114]N. Klimov, V. Podkovyrov, A. Zhitlukhin, D. Kovalenko, B. Bazylev, G. Janeschitz, I. Landman, S. Pestchanyi, G. Federici, A. Loarte, M. Merola, J. Linke, T. Hirai, and J. Compan, J. Nucl. Mater. **390-391**, 721 (2009).

[115]T. Loewenhoff, J. Linke, G. Pintsuk, C. Thomser, Fusion Eng. and Design **87**, 1201 (2012).

[116]I. E. Garkusha, A. N. Bandura, O. V. Byrka, V. V. Chebotarev, I. Landman, V. A. Makhlaj, S. Pestchanyi, and V. I. Tereshin, J. Nucl. Mater. **386-388**, 127 (2009).

[117]B. Lipschultz, D. Whyte, and B. LaBombard, Plasma Phys. Control. Fusion **47**, 1559 (2005).

[118]M. Wirtz, J. Linke, G. Pintsuk, L. Singheiser, and M. Zlobinski, J. Nucl. Mater. **438**, S833 (2013).

[119]T. Hirai, G. Pintsuk, J. Linke, and M. Batilliot, J. Nucl. Mater. **390-391**, 751 (2009).

[120]E. J. Doyle (Chair Transport Phys.), W. A. Houlberg (Chair Confinement Database & Modeling), Y. Kamada (Chair Pedestal & Edge), V. Mukhovatov (co-Chair Transport Phys.), T. H. Osborne (co-chair Pedestal & Edge), A. Polevoi (co-chair Confinement Database & Modeling), G. Bateman, J. W. Connor, J. G. Cordey (retired), T. Fujita, X. Garbet, T. S. Hahm, L. D. Horton, A. E. Hubbard, F. Imbeaux, F. Jenko, J. E. Kinsey, Y. Kishimoto, J. Li, T. C. Luce, Y. Martin, M. Ossipenko, V. Parail, A. Peeters, T. L. Rhodes, J. E. Rice, C. M. Roach, V. Rozhansky, F. Ryter, G. Saibene, R. Sartori, A. C. C. Sips, J. A. Snipes, M. Sugihara, E. J. Synakowski, H. Takenaga, T. Takizuka, K. Thomsen, M. R. Wade, H. R. Wilson, ITPA Transport Phys. Topical Group, ITPA Confinement Database & Modeling Group, and ITPA Pedestal & Edge

Topical Group, Nucl. Fusion **47**, S18 (2007).

[121]K. Tobita, S. Nishio, M. Sato, S. Sakurai, T. Hayashi, Y. K. Shibama, T. Isono, M. Enoeda, H. Nakamura, S. Sato, K. Ezato, T. Hayashi, T. Hirose, S. Ide, T. Inoue, Y. Kamada, Y. Kawamura, H. Kawashima, N. Koizumi, G. Kurita, Y. Nakamura, K. Mouri, T. Nishitani, J. Ohmori, N. Oyama, K. Sakamoto, S. Suzuki, T. Suzuki, H. Tanigawa, K. Tsuchiya, and D. Tsuru, Nucl. Fusion **47**, 892 (2007).

[122]K. Lackner, R. Andreani, D. Campbell, M. Gasparotto, D. Maisonnier, and M. A. Pick, J. Nucl. Mater. **307-311**, 10 (2002).

[123]F. Najmabadi, The ARIES Team, A. Abdou, L. Bromberg, T. Brown, V. C. Chan, M. C. Chu, F. Dahlgren, L. El-Guebaly, P. Heitzenroeder, D. Henderson, H. E. St John, C. E. Kessel, L. L. Lao, G. R. Longhurst, S. Malang, T. K. Mau, B. J. Merrill, R. L. Miller, E. Mogahed, R. L. Moore, T. Petrie, D. A. Petti, P. Politzer, A. R. Raffray, D. Steiner, I. Sviatoslavsky, P. Synder, G. M. Syaebler, A. D. Turnbull, M. S. Tillack, L. M. Waganer, X. Wang, P. West, and P. Wilson, Fusion Eng. Design **80**, 3 (2006).

[124]B. N. Kolbasov, V. A. Belyakov, E. N. Bondarchuk, A. A. Borisov, I. R. Kirillov, V. M. Leonov, G. E. Shatalov, Y. A. Sokolov, Y. S. Strebkov, and N. N. Vasiliev, Fusion Eng. Design **83**, 870 (2008).

[125]P. T. Lang, A. Loarte, G. Saibene, L. R. Baylor, M. Becoulet, M. Cavinato, S. Clement-Lorenzo, E. Daly, T. E. Evans, M. E. Fenstermacher, Y. Gribov, L. D. Horton, C. Lowry, Y. Martin, O. Neubauer, N. Oyama, M. J. Schaffer, D. Stork, W. Suttrop, P. Thomas, M. Tran, H. R. Wilson, A. Kavin, and O. Schmitz, Nucl. Fusion **53**, 043004 (2013).

[126]T. E. Evans, J. Nucl. Mater. **438**, S11 (2013).

[127]M. Becoulet, G. Huysmans, P. Thomas, E. Joffrin, F. Rimini, P. Monier-Garbet, A. Grosman, P. Ghendrih, V. Parail, P. Lomas, G. Matthews, H. Wilson, M. Gryaznevich, G. Counsell, A. Loarte, G. Saibene, R. Sartori, A. Leonard, P. Snyder, T. Evans, P. Gohil, R. Moyer, Y. Kamada, N. Oyama, T. Hatae, K. Kamiya, A. Degeling, Y. Martin, J. Lister, J. Rapp, C. Perez, P. Lang, A. Chankin, T. Eich, A. Sips, J. Stober, L. Horton, A. Kallenbach, W. Suttrop, S. Saarelma, S. Cowley, J. Lönnroth, M. Shimada, A. Polevoi, and G. Federici, J. Nucl. Mater. **337-339**, 677 (2005).

[128]N. Oyama, P. Gohil, L. D. Horton, A. E. Hubbard, J. W. Hughes, Y. Kamada, K. Kamiya, A. W. Leonard, A. Loarte, R. Maingi, G. Saibene, R. Sartori, J. K. Stober, W. Suttrop, H. Urano, W. P. West, and the ITPA Pedestal Topical Group, Plasma Phys. Control. Fusion **48**, A171 (2006).

[129]N. Oyama, J. Phys.: Conf. Ser. **123**, 012002 (2008).

[130]J. Stober, M. Maraschek, G. D. Conway, O. Gruber, A. Herrmann, A. C. C. Sips, W. Treutterer, H. Zohm, and the ASDEX Upgrade Team, Nucl. Fusion **41**, 1123 (2001).

[131]H. Zohm, Plasma Phys. Control. Fusion **38**, 105 (1996).

[132]G. Saibene, P. J. Lomas, R. Sartori, A. Loarte, J. Stober, Y. Andrew, S. A. Arshad, G. D. Conway, E. de la Luna, K. Günther, L. C. Ingesson, M. A. H. Kempenaars, A. Korotkov, H. R. Koslowski, J. S. Lönnroth, D. C. McDonald, A. Meigs, P. Monier-Garbet, V. Parail, C. P. Perez, F. G. Rimini, S. Sharapov, and P. R. Thomas, Nucl. Fusion **45**, 297 (2005).

[133]R. Satori, G. Saiben, L. D. Horton, M. Becoulet, R. Budny, D. Borba, A. Chankin, G. D. Conway, G. Cordey, D. McDonald, K. Guenther, M. G. von Hellermann, Yu Igithkanov A. Loarte, P. J. Lomas, O. Pogutse, and J. Rapp, Plasma Phys. Control. Fusion **46**, 723 (2004).

[134]T. H. Osborne, R. J. Groebner, L. L. Lao, and A. W. Leonard, Proc 24th EPS Conf. on Controlled Fusion and Plasma Physics (Berchtesgaden, Germany, 1997) (Petit-Lancy, Switzerland).

[135]R. Maingi, K. Tritz, E. D. Fredrickson, J. E. Menard, S. A. Sabbagh, D. Stutman, M. G. Bell, R. E. Bell, C. E. Bush, D. A. Gates, D. W. Johnson, R. Kaita, S. M. Kaye, H. W. Kugel, B. P. LeBlanc, D. Mueller, R. Raman, A. L. Roquemore, and V. A. Soukhanovskii, Nucl. Fusion **45**, 264 (2005).

[136]R. Maingi, M. G. Bell, E. D. Fredrickson, K. C. Lee, R. J. Maqueda, P. Snyder, K. Tritz, S. J. Zweben, R. E. Bell, T. M. Biewer, C. E. Bush, J. Boedo, N. H. Brooks, L. Delgado-Aparicio, C. W. Domier, D. A. Gates, D. W. Johnson, R. Kaita, S. M. Kaye, H. W. Kugel, B. P. LeBlanc, N. C. Luhmann, J. E. Menard, D. Mueller, H. Park, R. Raman, A. L. Roquemore, S. A. Sabbagh, V. A. Soukhanovskii, T. Stevenson, and D. Stutman, Phys. Plasmas **13**, 092510 (2006).

[137]D. A. Mossessian, P. B. Snyder, M. Greenwald, J. W. Hughes, Y. Lin, A. Mazurenko, S. Medvedev, H. R. Wilson, and S. Wolfe, Plasma Phys. Control. Fusion **44**, 423 (2002).

[138]Y. Takase, R. L. Boivin, F. Bombarda, P. T. Bonoli, C. Christiansen, C. Fiore, D. Garnier, J. A. Goetz, S. N. Golovato, R. Granetz, M. Greenwald, S. F. Horne, A. Hubbard, I. H. Hutchinson, J. Irby, B. LaBombard, B. Lipschultz, E. Marmar,

M. May, A. Mazurenko, G. McCracken, P. O'Shea, M. Porkolab, J. Reardon, J. Rice, C. Rost, J. Schachter, J. A. Snipes, P. Stek, J. Terry, R. Watterson, B. Welch, and S. Wolfe, Phys. Plasmas **4**, 1647 (1997).

[139]K. Kamiya, H. Kimura, H. Ogawa, H. Kawashima, K. Tsuzuki, M. Sato, Y. Miura, and JFT-2M Group, Nucl. Fusion **43**, 1214 (2003).

[140]R. Maingi, T. H. Osborne, B. P. LeBlanc, R. E. Bell, J. Manickam, P. B. Snyder, J. E. Menard, D. K. Mansfield, H. W. Kugel, R. Kaita, S. P. Gerhardt, S. A. Sabbagh, F. A. Kelly and the NSTX Research Team, Phys. Rev. Lett. **103**, 075001 (2009).

[141]R. Maingi, D. P. Boyle, J. M. Canik, S. M. Kaye, C. H. Skinner, J. P. Allain, M. G. Bell, R. E. Bell, S. P. Gerhardt, T. K. Gray, M. A. Jaworski, R. Kaita, H. W. Kugel, B. P. LeBlanc, J. Manickam, D. K, Mansfield, J. E. Menard, T. H. Osborne, R. Raman, A. L. Roquemore, S. A. Sabbagh, P. B. Snyder and V. A. Soukhanovskii, Nucl. Fusion **52**, 083001 (2012).

[142]J. M. Canik, R. Maingi, S. Kubota, Y. Ren, R. E. Bell, J. D. Callen, W. Guttenfelder, H. W. Kugel, B. P. LeBlanc, T. H. Osborne, and V. A. Soukhanovskii, Phys. Plasmas **18**, 056118 (2011).

[143]H. Q. Wang, G. S. Xu, H. Y. Guo, B. N. Wan, V. Naulin, S. Y. Ding, N. Yan, W. Zhang, L. Wang, S. C. Liu, R. Chen, L. M. Shao, H. Xiong, P. Liu, M. Hiang, and G.-N. Luo, Nucl. Fusion **52**, 123011 (2012).

[144]H. Y. Guo, J. Li, X. Z. Gong, B. N. Wan, J. S. Hu, L. Wang, H. Q. Wang, J. E. Menard, M. A. Jaworski, K. F. Gan, S. C. Liu, G. S. Xu, S. Y. Ding, L. Q. Hu, Y. F. Liang, J. B. Liu, G. N. Luo, H. Si, D. S. Wang, Z. W. Wu, L. Y. Xiang, B. J. Xiao, L. Zhang, X. L. Zou, D. L. Hillis, A. Loarte, R. Maingi and the EAST Team, Nucl.

Fusion **54**, 013002 (2014).

[145]J. Li, H. Y. Guo, B. N. Wan, X. Z. Gong, Y. F. Liang, G. S. Xu, K. F. Gan, J. S. Hu, H. Q. Wang, L. Wang, L. Zeng, Y. P. Zhao, P. Denner, G. L. Jackson, A. Loarte, R. Maingi, J. E. Menard, M. Rack, and X. L. Zou, Nature Phys. **9**, 817 (2013).

[146]D. G. Whyte, A. E. Hubbard, J. W. Hughes, B. Lipschultz, J. E. Rice, E. S. Marmar, M. Greenwald, I. Cziegler, A. Dominguez, T. Golfinopoulos, N. Howard, L. Lin, R. M. McDermott, M. Porkolab, M. L. Reinke, J. Terry, N. Tsujii, S. Wolfe, S. Wukitch, Y. Lin, and the Alcator C-Mod Team, Nucl. Fusion **50**, 105005 (2010).

[147]A. E. Hubbard, D. G. Whyte, R. M. Churchill, I. Cziegler, A. Dominguez, T. Golfinopoulos, J. W. Hughes, J. E. Rice, I. Bespamyatnov, M. J. Greenwald, N. Howard, B. Lipschultz, E. S. Marmar, M. L. Reinke, W. L. Rowan, J. L. Terry, and the Alcator C-Mod Group, Phys. Plasmas **18**, 056115 (2011).

[148]K. H. Burrell, A. M. Garofalo, W. M. Solomon, M. E. Fenstermacher, T. H. Osborne, J. K. Park, M. J. Schaffer, and P. B. Snyder, Phys. Plasmas **19**, 056117 (2012).

[149]W. Suttrop, M. Maraschek, G. D. Conway, H. U. Fahrbach, G. Haas, L. D. Horton, T. Kurki-Suonio, C. J. Lasnier, A. W. Leonard, C. F. Maggi, H. Meister, A. Mück, R. Neu, I. Nunes, T. Pütterich, M. Reich, A. C. C. Sips, and ASDEX Upgrade Team, Plasma Phys. Control. Fusion **45**, 1399 (2003).

[150]W. Suttrop, V. Hynönen, T. Kurki-Suonio, P. T. Lang, M. Maraschek, R. Neu, A. Stäbler, G. D. Conway, S. Hacquin, M. Kempenaars, P. J. Lomas, M. F. F. Nave, R. A. Pitts, K.-D. Zastrow, the ASDEX Upgrade Team, and Contributors to the JET-EFDA Workprogramme, Nucl. Fusion **45**, 721 (2005).

[151]Y. Sakamoto, H. Shirai, T. Fujita, S. Ide, T. Takizuka, N. Oyama, and Y. Kamada,

Plasma Phys. Control. Fusion **46**, A299 (2004).

[152]N. Oyama, Y. Sakamoto, A. Isayama, M. Takechi, P. Gohil, L. L. Lao, P. B. Snyder, T. Fujita, S. Ide, Y. Kamada, Y. Miura, T. Oikawa, T. Suzuki, H. Takenaga, K. Toi, and the JT-60 Team, Nucl. Fusion **45**, 871 (2005).

[153]P. B. Snyder, K. H. Burrell, H. R. Wilson, M. S. Chu, M. E. Fenstermacher, A. W. Leonard, R. A. Moyer, T. H. Osborne, M. Umansky, W. P. West, and X. Q. Xu, Nucl. Fusion **47**, 961 (2007).

[154]P. B. Snyder, T. H. Osborne, K. H. Burrell, R. J. Groebner, A. W. Leonard, R. Nazikian, D. M. Orlov, O. Schmitz, M. R. Wade, and H. R. Wilson, Phys. Plasmas **19**, 056115 (2012).

[155]P. T. Lang, G. D. Conway, T. Eich, L. Fattorini, O. Gruber, S. Günter, L. D. Horton, S. Kálvin, A. Kallenbach, M. Kaufmann, G. Kocsis, A. Lorenz, M. E. Manso, M. Maraschek, V. Mertens, J. Neuhauser, I. Nunes, W. Schneider, W. Suttrop, H. Urano, and the ASDEX Upgrade Team, Nucl. Fusion **44**, 665 (2004).

[156]P. T. Lang, D. Frigione, A. Géraud, T. Alarcon, P. Bennett, G. Cseh, D. Garnier, L. Garzotti, F. Köchl, G. Kocsis, M. Lennholm, R. Neu, R. Mooney, S. Saarelma, B. Sieglin, JET EFDA Contributors, Nucl. Fusion **53**, 073010 (2013).

[157]L. R. Baylor, N. Commaux, T. C. Jernigan, S. J. Meitner, S. K. Combs, R. C. Isler, E. A. Unterberg, N. H. Brooks, T. E. Evans, A. W. Leonard, T. H. Osborne, P. B. Parks, P. B. Snyder, E. J. Strait, M. E. Fenstermacher, C. J. Lasnier, R. A. Moyer, A. Loarte, G. T. A. Huijsmans, and S. Futatani, Phys. Plasmas **20**, 082513 (2013).

[158]T. Rhee, J. M. Kwon, P. H. Diamond, and W. W. Xiao, Phys. Plasmas **19**, 022505 (2012).

[159]W. W. Xiao, P. H. Diamond, X. L. Zou, J. Q. Dong, X. T. Ding, L. H. Yao, B. B. Feng, C. Y. Chen, W. L. Zhong, M. Xu, B. S. Yuan, T. Rhee, J. M. Kwon, Z. B. Shi, J. Rao, G. J. Lei, J. Y. Cao, J. Zhou, M. Huang, D. L. Yu, Y. Huang, K. J. Zhao, Z. Y. Cui, X. M. Song, Y. D. Gao, Y. P. Zhang, J. Cheng, X. Y. Han, Y. Zhou, Y. B. Dong, X. Q. Ji, Q. W. Yang, Y. Liu, L. W. Yan, X. R. Duan, Y. Liu, the HL-2A Team, Nucl. Fusion **52**, 114027 (2012).

[160]J. Kim, Y. M. Jeon, W. W. Xiao, S. W. Yoon, J. K. Park, G. S. Yun, J.-W. Ahn, H. S. Kim, H. L. Yang, H. K. Kim, S. Park, J. H. Jeong, M. Jung, G. H. Choe, W. H. Ko, S. G. Lee, Y. U. Nam, J. G. Bak, K. D. Lee, H. K. Na, S. H. Hahn, P. H. Diamond, T. Rhee, J. M. Kwon, S. A. Sabbagh, Y. S. Park, H. K. Park, Y. S. Na, W. C. Kim, J. G. Kwak, the KSTAR contributors, Nucl. Fusion **52**, 114011 (2012).

[161]J.-G. Kwak, Y. K. Oh, H. L. Yang, K. R. Park, Y. S. Kim, W. C. Kim, J. Y. Kim, S. G. Lee, H. K. Na, M. Kwon, G. S. Lee, H. S. Ahn, J.-W. Ahn, Y. S. Bae, J. G. Bak, E. N. Bang, C. S. Chang, D. H. Chang, Z. Y. Chen, K. W. Cho, M. H. Cho, M. Choi, W. Choe, J. H. Choi, Y. Chu, K. S. Chung, P. Diamond, L. Delpech, H. J. Do, N. Eidietis, A. C. England, R. Ellis, T. Evans, G. Choe, L. Grisham, Y. Gorelov, H. S. Hahn, S. H. Hahn, W. S. Han, T. Hatae, D. Hillis, T. Hoang, J. S. Hong, S. H. Hong, S. R. Hong, J. Hosea, D. Humphreys, Y. S. Hwang, A. Hyatt, K. Ida, Y. K. In, S. Ide, Y. B. Jang, Y. M. Jeon, J. I. Jeong, N. Y. Jeong, S. H. Jeong, J. K. Jin, M. Joung, J. Ju, K. Kawahata, C. H. Kim, H.-S. Kim, H. S. Kim, H. J. Kim, H. K. Kim, H. T. Kim, J. H. Kim, J. Kim, J. C. Kim, J.-S. Kim, J.-S. Kim, K.-M. Kim, K. J. Kim, K. P. Kim, M. K. Kim, S. T. Kim, S. W. Kim, Y. J. Kim, Y. K. Kim, Y. O. Kim, J. S. Ko, W. H. Ko, Y. Kogi, E. Kolemen, J. D. Kong, S. W. Kwak, J. M. Kwon, O. J. Kwon, D. G.

Lee, D. R. Lee, D. S. Lee, H. J. Lee, J. Lee, J. H. Lee, K. D. Lee, K. S. Lee, S. H. Lee, S. I. Lee, S. M. Lee, T. G. Lee, W. Lee, W. L. Lee, D. S. Lim, X. Litaudon, J. Lohr, D. Mueller, K. M. Moon, D. H. Na, Y. S. Na, Y. U. Nam, W. Namkung, K. Narihara, S. T. Oh, D. G. Oh, T. Ono, B. H. Park, D. S. Park, G. Y. Park, H. Park, H. T. Park, J. K. Park, J. S. Park, M. K. Park, S. H. Park, S. Park, Y. M. Park, Y. S. Park, R. Parker, D. R. Rhee, S. A. Sabbagh, K. Sakamoto, S. Shiraiwa, D. C. Seo, S. H. Seo, J. C. Seol, Y. J. Shi, S. H. Son, N. H. Song, T. Suzuki, L. Terzolo, M. Walker, G. Wallace, K. Watanabe, S. J. Wang, H. J. Woo, I. S. Woo, M. Yagi, Y. W. Yu, I. Yamada, Y. Yonekawa, C. M. Yoo, K. I. You, J. W. Yoo, G. S. Yun, M. G. Yu, S. W. Yoon, W. Xiao, S. Zoletnik, the KSTAR Team, Nucl. Fusion **53**, 104005 (2013).

[162]A. W. Degeling, Y. R. Martin, J. B. Lister, L. Villard, V. N. Dokouka, V. E. Lukash, and R. R. Khayrutdinov, Plasma Phys. Control. Fusion **45**, 1637 (2003).

[163]E. de la Luna, F. Sartori, P. Lomas, and G. Saibene, Proc 23rd Int. Conf. on Fusion Energy 2010 (Daejon, South Korea, 2010) (Vienna: IAEA).

[164]S. H. Kim, M. M. Cavinato, V. Dokuka, A. A. Ivanov, R. R. Khayrutdinov, P. T. Lang, J. B. Lister, V. E. Lukash, Y. R. Martin, S. Y. Medvedev, and L. Villard, Plasma Phys. Control. Fusion **51**, 055021 (2009).

[165]P. T. Lang, A. W. Degeling, J. B. Lister, Y. R. Martin, P. J. M. Carthy, A. C. C. Sips, W. Suttrop, G. D. Conway, L. Fattorini, O. Gruber, L. D. Horton, A. Herrmann, M. E. Manso, M. Maraschek, V. Mertens, A. Mück, W. Schneider, C. Sihler, W. Treutterer, H. Zohm, and ASDEX Upgrade Team, Plasma Phys. Control. Fusion **46**, L31 (2004).

[166]J. M. Canik, R. Maingi, T. E. Evans, R. E. Bell, S. P. Gerhardt, H. W. Kugel, B. P. LeBlanc, J. Manickam, J. E. Menard, T. H. Osborne, J. K. Park, S. Paul, P. B. Snyder,

S. A. Sabbagh, E. A. Unterberg, the NSTX Team, Nucl. Fusion **50**, 034012 (2010).

[167]J. M. Canik, A. C. Sontag, R. Maingi, R. Bell, D. A. Gates, S. P. Gerhardt, H. W. Kugel, B. P. LeBlanc, J. Menard, S. Paul, S. Sabbagh, and V. A. Soukhanovskii, Nucl. Fusion **50**, 064016 (2010).

[168]P. T. Lang, J. Neuhauser, L. D. Horton, T. Eich, L. Fattorini, J. C. Fuchs, O. Gehre, A. Herrmann, P. Ignácz, M. Jakobi, S. Kálvin, M. Kaufmann, G. Kocsis, B. Kurzan, C. Maggi, M. E. Manso, M. Maraschek, V. Mertens, A. Mück, H. D. Murmann, R. Neu, I. Nunes, D. Reich, M. Reich, S. Saarelma, W. Sandmann, J. Stober, U. Vogl, and the ASDEX Upgrade Team, Nucl. Fusion **43**, 1110 (2003).

[169]S. Futatani, G. Huijsmans, A. Loarte, L. R. Baylor, N. ommaux, T. C. Jernigan, M. E. Fenstermacher, C. Lasnier, T. H. Osborne, and B. Pegourié, Proc. 24th Int. Conf. on Fusion Energy 2012 (San Diego, CA, 2012) (Vienna:IAEA) ITR/P1-22.

[170]C. Neumeyer, Fusion Sci. Technol. **60**, 95 (2011).

[171]T. E. Evans, M. E. Fenstermacher, R. A. Moyer, T. H. Osborne, J. G. Watkins, P. Gohil, I. Joseph, M. J. Schaffer, L. R. Baylor, M. Becoulet, J. A. Boedo, K. H. Burrell, J. S. deGrassie, K. H. Finken, T. Jernigan, M. W. Jakubowski, C. J. Lasnier, M. Lehnen, A. W. Leonard, J. Lönnroth, E. Nardon, V. Parail, O. Schmitz, B. Unterberg, and W. P. West, Nucl. Fusion **48**, 024002 (2008).

[172]K. H. Burrell, T. E. Evans, E. J. Doyle, M. E. Fenstermacher, R. J. Groebner, A. W. Leonard, R. A. Moyer, T. H. Osborne, M. J. Schaffer, P. B. Snyder, P. R. Thomas, W. P. West, J. A. Boedo, A. M. Garofalo, P. Gohil, G. L. Jackson, R. J. La Haye, C. J. Lasnier, H. Reimerdes, T. L. Rhodes, J. T. Scoville, W. M. Solomon, D. M. Thomas, G. Wang, J. G. Watkins, and L. Zeng, Plasma Phys. Control. Fusion **47**, B37 (2005).

[173]T. E. Evans and the DIII-D Team, Plasma and Fusion Research **7**, 2402046 (2012).

[174]G. R. McKee, Z. Yan, C. Holland, R. J. Buttery, T. E. Evans, R. A. Moyer, S. Mordijck, R. Nazikian, T. L. Rhodes, O. Schmitz, and M. R. Wade, Nucl. Fusion **53**, 113011 (2013).

[175]M. J. Lanctot, R. J. Buttery, J. S. deGrassie, T. E. Evans, N. M. Ferraro, J. M. Hanson, S. R. Haskey, R. A. Moyer, R. Nazikian, T. H. Osborne, D. M. Orlov, P. B. Snyder, M. R. Wade, and the DIII-D Team, Nucl. Fusion **53**, 083019 (2013).

[176]Y. Liang, H. Koslowski, P. Thomas, E. Nardon, B. Alper, P. Andrew, Y. Andrew, G. Arnoux, Y. Baranov, M. Becoulet, M. Beurskens, T. Biewer, M. Bigi, K. Crombe, E. de la Luna, P. de Vries, W. Fundamenski, S. Gerasimov, C. Giroud, M. Gryaznevich, N. Hawkes, S. Hotchin, D. Howell, S. Jachmich, V. Kiptily, L. Moreira, V. Parail, S. Pinches, E. Rachlew, and O. Zimmermann, Phys. Rev. Lett. **98**, 265004 (2007).

[177]Y. Liang, H. R. Koslowski, P. R. Thomas, E. Nardon, S. Jachmich, B. Alper, P. Andrew, Y. Andrew, G. Arnoux, Y. Baranov, M. Becoulet, M. Beurskens, T. Biewer, M. Bigi, K. Crombe, E. de la Luna, P. de Vries, T. Eich, H. G. Esser, W. Fundamenski, S. Gerasimov, C. Giroud, M. P. Gryaznevich, D. Harting, N. Hawkes, S. Hotchin, D. Howell, A. Huber, M. Jakubowski, V. Kiptily, A. Kreter, L. Moreira, V. Parail, S. D. Pinches, E. Rachlew, O. Schmitz, O. Zimmermann, JET EFDA Contributors, Plasma Phys. Control. Fusion **49**, B581 (2007).

[178]Y. M. Jeon, J. K. Park, S. W. Yoon, W. H. Ko, S. G. Lee, K. D. Lee, G. S. Yun, Y. U. Nam, W. C. Kim, J.-G. Kwak, K. S. Lee, H. K. Kim, H. L. Yang, KSTAR Team, Phys. Rev. Lett. **109**, 035004 (2012).

[179]A. Kirk, Y. Liu, E. Nardon, P. Tamain, P. Cahyna, I. Chapman, P. Denner, H. Meyer, S. Mordijck, D. Temple, the MAST Team, Plasma Phys. Control. Fusion **53**, 065011 (2011).

[180]A. Kirk, I. T. Chapman, Y. Liu, P. Cahyna, P. Denner, G. Fishpool, C. J. Ham, J. R. Harrison, Y. Liang, E. Nardon, S. Saarelma, R. Scannell, A. J. Thornton, the MAST Team, Nucl. Fusion **53**, 043007 (2013).

[181]A. Kirk, E. Nardon, P. Tamain, P. Denner, H. Meyer, S. Mordijck, D. Temple, and the MAST Team, J. Nucl. Mater. **415**, S910 (2011).

[182]W. Suttrop, T. Eich, J. C. Fuchs, S. Günter, A. Janzer, A. Herrmann, A. Kallenbach, P. T. Lang, T. Lunt, M. Maraschek, R. M. McDermott, A. Mlynek, T. Pütterich, M. Rott, T. Vierle, E. Wolfrum, Q. Yu, I. Zammuto, H. Zohm, ASDEX Upgrade Team, Phys. Rev. Lett. **106**, 225004 (2011).

[183]W. Suttrop, L. Barrera, A. Herrmann, R. M. McDermott, T. Eich, R. Fischer, B. Kurzan, P. T. Lang, A. Mlynek, T. Pütterich, S. K. Rathgeber, M. Rott, T. Vierle, E. Viezzer, M. Willensdorfer, E. Wolfrum, I. Zammuto, the ASDEX Upgrade Team, Plasma Phys. Control. Fusion **53**, 124014 (2011).

[184]U. Stroth, J. Adamek, L. Aho-Mantila, S. Äkäslompolo, C. Amdor, C. Angioni, M. Balden, S. Bardin, L. Barrera Orte, K. Behler, E. Belonohy, A. Bergmann, M. Bernert, R. Bilato, G. Birkenmeier, V. Bobkov, J. Boom, C. Bottereau, A. Bottino, F. Braun, S. Brezinsek, T. Brochard, M. Brüdgam, A. Buhler, A. Burckhart, F. J. Casson, A. Chankin, I. Chapman, F. Clairet, I. G. J. Classen, J. W. Coenen, G. D. Conway, D. P. Coster, D. Curran, F. da Silva, P. de Marné, R. D'Inca, D. Douai, R. Drube, M. Dunne, R. Dux, T. Eich, H. Eixenberger, N. Endstrasser, K. Engelhardt,

B. Esposito, E. Fable, R. Fischer, H. Fünfgelder, J.C. Fuchs, K. Gál, M. García Muñoz, B. Geiger, L. Giannone, T. Görler, S. da Graca, H. Greuner, O. Gruber, A. Gude, L. Guimarais, S. Günter, G. Haas, A.H. Hakola, D. Hangan, T. Happel, T. Härtl, T. Hauff, B. Heinemann, A. Herrmann, J. Hobirk, H. Höhnle, M. Hölzl, C. Hopf, A. Houben, V. Igochine, C. Ionita, A. Janzer, F. Jenko, M. Kantor, C. P. Käsemann, A. Kallenbach, S. Kálvin, A. Kappatou, O. Kardaun, W. Kasparek, M. Kaufmann, A. Kirk, H. J. Klingshirn, M. Kocan, G. Kocsis, C. Konz, R. Koslowski, K. Krieger, M. Kubic, T. Kurki-Suonio, B. Kurzan, K. Lackner, P. T. Lang, P. Lauber, M. Laux, A. Lazaros, F. Leipold, F. Leuterer, S. Lindig, S. Lisgo, A. Lohs, T. Lunt, H. Maier, T. Makkonen, K. Mank, M. E. Manso, M. Maraschek, M. Mayer, P. J. McCarthy, R. McDermott, F. Mehlmann, H. Meister, L. Menchero, F. Meo, P. Merkel, R. Merkel, V. Mertens, F. Merz, A. Mlynek, F. Monaco, S. Müller, H. W. Müller, M. Münich, G. Neu, R. Neu, D. Neuwirth, M. Nocente, B. Nold, J. M. Noterdaeme, G. Pautasso, G. Pereverzev, B. Plöckl, Y. Podoba, F. Pompon, E. Poli, K. Polozhiy, S. Potzel, M. J. Püschel, T. Pütterich, S. K. Rathgeber, G. Raupp, M. Reich, F. Reimold, T. Ribeiro, R. Riedl, V. Rohde, G. V. Rooij, J. Roth, M. Rott, F. Ryter, M. Salewski, J. Santos, P. Sauter, A. Scarabosio, G. Schall, K. Schmid, P. A. Schneider, W. Schneider, R. Schrittwieser, M. Schubert, J. Schweinzer, B. Scott, M. Sempf, M. Sertoli, M. Siccinio, B. Sieglin, A. Sigalov, A. Silva, F. Sommer, A. Stäbler, J. Stober, B. Streibl, E. Strumberger, K. Sugiyama, W. Suttrop, T. Tala, G. Tardini, M. Teschke, C. Tichmann, D. Told, W. Treutterer, M. Tsalas, M. A. Van Zeeland, P. Varela, G. Veres, J. Vicente, N. Vianello, T. Vierle, E. Viezzer, B. Viola, C. Vorpahl, M. Wachowski, D. Wagner, T. Wauters, A. Weller, R. Wenninger, B. Wieland,

M. Willensdorfer, M. Wischmeier, E. Wolfrum, E. Würsching, Q. Yu, I. Zammuto, D. Zasche, T. Zehetbauer, Y. Zhang, M. Zilker, and H. Zohm, Nucl. Fusion **53**, 104003 (2013).

[185]D. Reiser and D. Chandra, Phys. Plasmas **16**, 042317 (2009).

[186]H. R. Strauss, L. Sugiyama, G. Y. Park, C. S. Chang, S. Ku, and I. Joseph, Nucl. Fusion **49**, 055025 (2009).

[187]M. Becoulet, G. Huysmans, X. Garbet, E. Nardon, D. Howell, A. Garofalo, M. Schaffer, T. Evans, K. Shaing, A. Cole, J.K. Park, and P. Cahyna, Nucl. Fusion **49**, 085011 (2009).

[188]N. M. Ferraro, T. E. Evans, L. L. Lao, R. A. Moyer, R. Nazikian, D. M. Orlov, M. W. Shafer, E. A. Unterberg, M. R. Wade, and A. Wingen, Nucl. Fusion **53**, 073042 (2013).

[189]M. R. Wade, Proc 24th Int. Conf on Fusion Energy (San Diego (2012).

[190]J. D. Callen, C. C. Hegna, and A. J. Cole, Nucl. Fusion **53**, 113015 (2013).

[191]J. D. Callen, A. J. Cole, C. C. Hegna, S. Mordijck, and R. A. Moyer, Nucl. Fusion **52**, 114005 (2012).

[192]T. M. Wilks, W. M. Stacey, and T. E. Evans, Phys. Plasmas **20**, 052505 (2013).

[193]S. Mordijck, E. J. Doyle, G. R. McKee, R. A. Moyer, T. L. Rhodes, L. Zeng, N. Commaux, M. E. Fenstermacher, K. W. Gentle, H. Reimerdes, O. Schmitz, W. M. Solomon, G. M. Staebler, and G. Wang, Phys. Plasmas **19**, 056503 (2012).

Figure Captions

Fig. 1. H-mode discharge in DIII-D with (a) plasma current and auxiliary heating power, (b) plasma stored energy, (c) edge pedestal electron pressure, (d) peak divertor heat flux. Note the increase in plasma stored energy after the H-mode transition, periodic growth and relaxation of the edge pressure, and periodic bursts of heat flux to the divertor target.

Fig. 2. (a) The edge perpendicular rotation profile given by $E_{\mathrm{r}} \times B$ in H-mode and L-mode. (b) The edge pressure profile in H-mode and L-mode.

Fig. 3. The edge H-mode profiles of (a) electron density, and (b) electron temperature measured by Thomson scattering in DIII-D. L-mode profiles are also shown for contrast.

Fig. 4. The edge H-mode current density with the calculated bootstrap current based on the profiles of Fig. 2. The L-mode profile is shown for contrast.

Fig. 5. Stability space for the H-mode pedestal as a function of pressure gradient and edge current.

Fig. 6. Pedestal stability diagrams for experiments on (a) ASDEX-Upgrade, (b) DIII-D, (c) JET and (d) JT-60U, showing Type I ELMs occurring near the stability bound while other types of discharges can lie in the stable region. [Reprinted courtesy of Institute of Publishing, P.B. Snyder, *et al.*, P.B. Snyder, *et al.*, Nucl. Fusion **49**, 085035 (2009) by permission.][22]

Fig. 7. The eigenmode structure calculated by ELITE for the unstable $n = 10$ mode in a typical DIII-D H-mode discharge. [Reprinted courtesy of Institute of Publishing, P.B. Snyder, *et al*., Plasma Phys. Controlled Fusion **46**, A131 (2004) by permission.][24]

Fig. 8. JET measurements with high time resolution of the MHD activity, pedestal temperature, and soft x-ray emission collapse, and outer divertor D_α emission and inner divertor x-ray bremsstrahlung from hot electron impact during a large Type I ELM. The collapse of the pedestal and intense inner divertor bremsstrahlung emission occur over a time interval of 200–300 μs, similar to the period of large MHD activity. [Reprinted courtesy of Institute of Publishing, A. Loarte, *et al*., Plasma Phys. Controlled Fusion **45**, 1549 (2003) by permission.][26]

Fig. 9. Profiles of (a) n_e and (b) T_e in DIII-D from Thomson scattering as fit before and after an ELM. The relative change in (c) n_e and (d) T_e due to an ELM. The profiles are collected over several ELMs and coherently averaged. [Reprinted courtesy of Institute of Publishing, A.W. Leonard, *et al*., Plasma Phys. Controlled Fusion **44**, 945 (2002) by permission.][34]

Fig. 10. Measured profiles in DIII-D of (a) n_{C+6}, (b) T_i, (c) v_θ, (d) v_ϕ, (e) n_e and (f) T_e just before (black) and after (gray) an ELM versus normalized radius. [Reprinted with permission from M.R. Wade, *et al*., Phys. Plasmas **12**, 056120 (2005). Copyright 2005 American Institute of Physics.][37]

Fig. 11. Radial profiles of E_r measured at various times on DIII-D during an ELM cycle: (a) $-1 \le t - t_{ELM}$ (ms) ≤ 0.5, (b) $0.5 \le t - t_{ELM}$ (ms) ≤ 3, and (c) $4 \le t - t_{ELM}$ (ms) ≤ 8.

[Reprinted with permission from M.R. Wade, *et al.*, Phys. Plasmas **12**, 056120 (2005). Copyright 2005 American Institute of Physics.][37]

Fig. 12. The LFS midplane pedestal density profile before and after an ELM from fast microwave reflectometry on ASDEX-Upgrade. [Reprinted courtesy of Institute of Publishing, I. Nunes, *et al.*, Nucl. Fusion **44**, 883 (2004) by permission.][40]

Fig. 13. Time delay of pedestal density drop at HFS midplane compared to LFS midplane as measured by fast microwave reflectometry in ASDEX-Upgrade. [Reprinted courtesy of Institute of Publishing, I. Nunes, *et al.*, Nucl. Fusion **44**, 883 (2004) by permission.][40]

Fig. 14. Normalized ELM energy loss ($\Delta W_{\mathrm{ELM}}/W_{\mathrm{ped}}$) vs pedestal plasma collisionality for a large range of Type I ELMing H-mode plasmas in ASDEX-Upgrade, DIII-D, JT-60U and JET. [Reprinted courtesy of Institute of Publishing, A. Loarte, *et al.*, Plasma Phys. Controlled Fusion **45**, 1549 (2003) by permission.][26]

Fig. 15. (a) The normalized convected ELM energy as measured by the Thomson scattering profile vs the pedestal density normalized by the Greenwald parameter, $n_{\mathrm{e,ped}}/n_{\mathrm{GW}}$, shows no clear density dependence in DIII-D. (b) The normalized conducted ELM energy vs the normalized pedestal density shows a strong decreasing tend with increasing density. [Reprinted with permission from A.W. Leonard, *et al.*, Phys. Plasmas **10**, 1765 (2003). Copyright 2003 American Institute of Physics.][48]

Fig. 16. The maximum of the temperature and heat flux density for an average ELM in the JET MKIIGB divertor. The ELM rise time derived by the fast temperature (or heat flux) rise is 390 μs on the outer target. The small increase of temperature and heat flux

prior to the ELM is not taken into account. [Reprinted courtesy of Elsevier Science Global, T. Eich, *et al.*, J. Nucl. Mater. **313-316**, 919 (2003).][50]

Fig. 17. Characteristic time scale of the ELM divertor power deposition, t_{IR}, on the outer divertor target vs transit time, $t_{||}^{conv}$, for various divertor tokamak experiments operating in a range of conditions, calculated for the pedestal plasma parameters. [Reprinted courtesy of Institute of Publishing, A. Loarte, *et al.*, Nucl. Fusion **47**, S203 (2007) by permission.][53]

Fig. 18. Time dependence of simulated (a) electron heat flux, q_e, ion heat flux, q_i, (b) sheath transmission factors, and (c) electron temperature T_e and ion temperature T_i, for a 120 kJ ELM on JET. Parameters τ_i and τ_e are the ion and electron timescales for propagation down the SOL from the upstream point at which the ELM disturbance is launched. Also shown in (a) is the target power obtained if constant sheath transmission factor, $\gamma = 8$ is assumed. [Reprinted courtesy of Institute of Publishing, R.A. Pitts, *et al.*, Nucl. Fusion **47**, 1437 (2007) by permission.][56]

Fig. 19. Divertor ELM energy fraction vs normalized ELM energy for JET's DOC-L configuration. I_p and B_ϕ in MA and T respectively. The "GB" marked data in the JET MKGIIB divertor configuration. [Reprinted courtesy of Institute of Publishing, R.A. Pitts, *et al.*, Nucl. Fusion **47**, 1437 (2007) by permission.][56]

Fig. 20. The Type I ELM energy deposition asymmetry in favor of the inner target is shown for the standard toroidal field direction in the JET MarkII SRP gas box divertor. A few discharges with toroidal field in the reversed direction exhibit a different trend. The

line corresponding to $E_{\mathrm{ELM,o}}/E_{ELM,i} = 1/2$ and 2 are shown for comparative purposes. [Reprinted courtesy of Institute of Publishing, R.A. Pitts, *et al.*, Nucl. Fusion **47**, 1437 (2007) by permission.][56]

Fig. 21. Effective wetted area during an ELM event and prior to the ELM event. The wetted area is calculated by dividing the tile integrated power flux (MW) by the maximum local heat flux (MW/m^2). For small ELMs little broadening is observed with values around 1.4. and for larger ELMs a significant broadening of about 4.3 is found when compared to the inter-ELM values prior to the ELM event. [Reprinted courtesy of Elsevier Science Global, T. Eich, *et al.*, J. Nucl. Mater. **415**, S856 (2011).][68]

Fig. 22. High speed video image in visible light of the MAST plasma obtained at the start of an ELM. The bright filaments are parallel to the background magnetic field.

Fig. 23. Inserted Langmuir probe measurement of a JET ELM. Show are the time evolution of (a) J_{sat} and (b) and effective radial $E \times B$ velocity. [Reprinted courtesy of Elsevier Science Global, C. Silva, *et al.*, J. Nucl. Mater. **337-339**, 722 (2005).][77]

Fig. 24. The heat flux pattern in ASDEX-Upgrade during an ELM. The region shown is just outside of the outboard strike point peak heat flux. In the left image the $B \times \nabla B$ direction point away from the X-point, while the right image the $B \times \nabla B$ direction points toward the X-point. [Reprinted courtesy of Institute of Publishing, T. Eich, *et al.*, Plasma Phys. Controlled Fusion **47**, 815 (2005) by permission.][85]

Fig. 25. Radial variation of the ELM peak density and temperature values obtained from inserted probes in DIII-D for (a) high density and (b) low density discharges. The

temperature decays quickly with radius in both cases, but the density decay length is much longer at low density. [Reprinted with permission from J.A. Boedo, *et al.*, Phys. Plasmas **12**, 072516 (2005). Copyright 2005 American Institute of Physics.][79]

Fig. 26. BOUT simulation of a DIII-D ELM. Contour plots of the normalized density perturbation ($\delta n/n_0$) along the outer midplane at early times (a) shows the expected peeling-ballooning structure ($n = 20$) in the pedestal region. Later (b) a fast radial burst across the separatrix, localized toroidally, but extended along the field. [Reprinted with permission from P.B. Snyder, *et al.*, Phys. Plasmas **12**, 056115 (2005). Copyright 2005 American Institute of Physics.][97]

Fig. 27. Simulation of a DIII-D ELM with the M3D code. Surface of constant temperature located inside the plasma, colored according to values of the poloidal magnetic flux representing minor radius, and a single magnetic field line started near the surface and traced in the lower X-point unstable (B_T) direction. The cut plane shows equally spaced temperature contours, tilted up to show the bottom of the plasma. [Reprinted with permission from L.E. Sugiyama, *et al.*, Phys. Plasmas **17**, 062505 (2010). Copyright 2010 American Institute of Physics.][98]

Fig. 28. Poincairè plot of the perturbed magnetic field and heat flux at the target at the time of the maximum magnetic energy perturbation for JOREK simulation of a JET-like 3 MA plasma. [Reprinted courtesy of Institute of Publishing, G.T.A. Huijsmans and A. Loarte, Nucl. Fusion **53**, 123023 (2013) by permission.][101]

Fig. 29. Expected main plasma ELM energy loss (ΔW_{ELM}) for uncontrolled ELMs and required ΔW_{ELM} for controlled ELMs in ITER vs plasma current (I_p) for a range of assumptions regarding the effective area for ELM energy deposition (A_{ELM}) and two assumptions regarding the change of safety factor with I_p (constant q_{95} or constant B_T). [Reprinted courtesy of Institute of Publishing, A. Loarte, *et al.*, Nucl. Fusion **54**, 033007 (2014) by permission.][108]

Fig. 30. Time history of long pulse QH-mode in DIII-D discharge with counter-I_p neutral beam injection. (a) Plasma current and divertor D_α emission, (b) amplitude of the edge magnetic field from the dominant $n = 2$ toroidal harmonic of the EHO, line-averaged density, (d) injected neutral beam power and total radiated power, and (e) neutral beam torque. NBI torque is negative when the torque is in the counter-I_p direction. [Reprinted with permission from K.H. Burrell, *et al.*, Phys. Plasmas **19**, 056117 (2012). Copyright 2012 American Institute of Physics.][148]

Fig. 31. (a) Peeling-ballooning stability diagram for a model DIII-D discharge showing the effect of density (collisionality) on the discharge trajectory, and density required to access the proposed QH region (shaded blue). (b) The same diagram for ITER indicating pedestal density required for QH-mode access. [Reprinted courtesy of Institute of Publishing, P.B. Snyder, *et al.*, Nucl. Fusion **47**, 961 (2007) by permission.][153]

Fig. 32. Onset of pellet pacing sequence in ASDEX-Upgrade: the ELM frequency follows immediately the pellet rate resulting in a ~threefold increase of the frequency and a corresponding ELM energy loss reduction. Additional convective losses associated with the expulsion of pellet injected particles (fuelling size pellets are used in this experiment)

cause a mild confinement loss. [Reprinted courtesy of Institute of Publishing, P.T. Lang, *et al.*, Nucl. Fusion **53**, 043004 (2013) by permission.][125]

Fig. 33. ELM suppression with RMP coils on DIII-D. Shown are (a) lower divertor D_α response to the RMP at high triangularity, $\delta = 0.53$, (b) lower D_α response to the RMP at low triangularity, $\delta = 0.26$, (c) q_{95} evolution at high triangularity (black) and low triangularity (grey), (d) timing and amplitude of the RMP coil current, (e) evolution of the pedestal electron collisionality, (f) energy confinement H-factor, and (g) total stored energy. The expected ITER collisionality (e) and confinement (f) are shown for comparison. [Reprinted courtesy of Institute of Publishing, T.E. Evans, *et al.*, Nucl. Fusion **48**, 024002 (2008) by permission.][171]

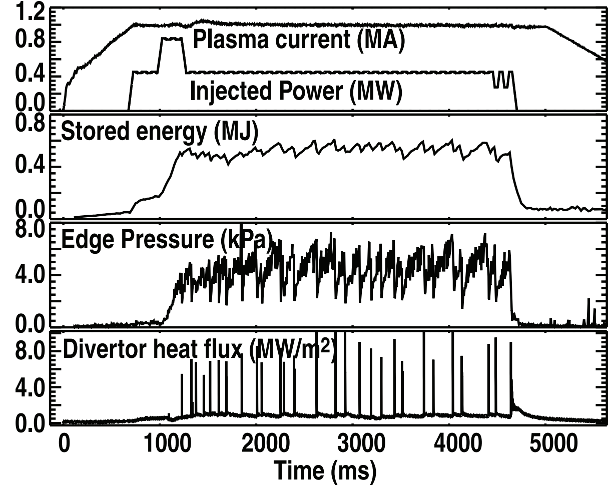

A.W. Leonard Figure 1

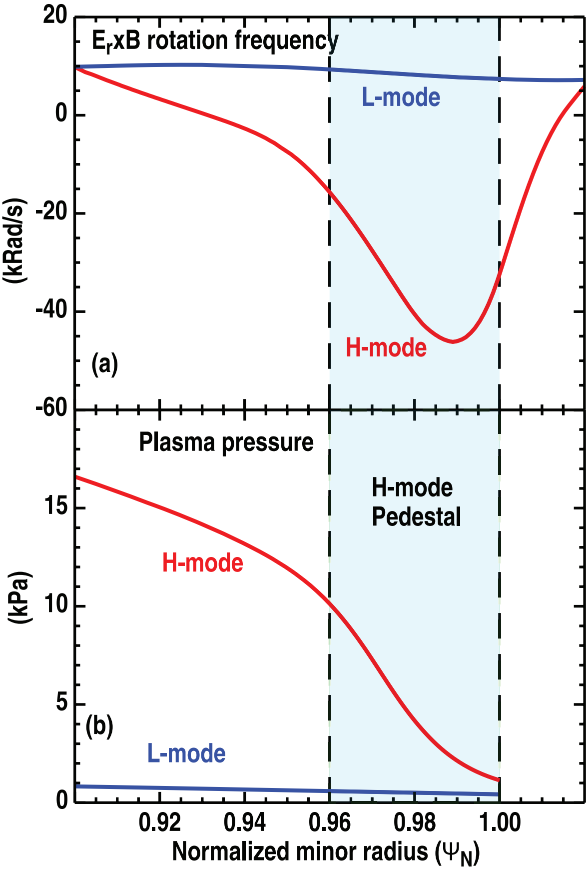

A.W. Leonard Figure 2

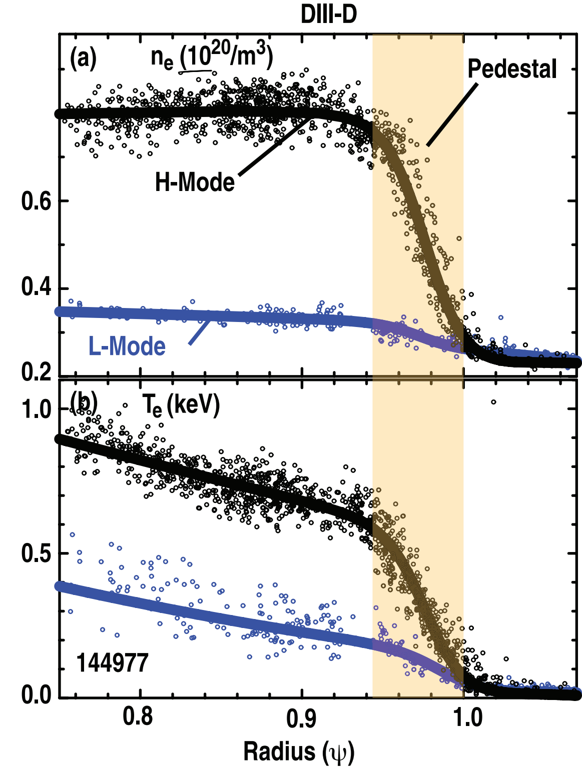

A.W. Leonard Figure 3

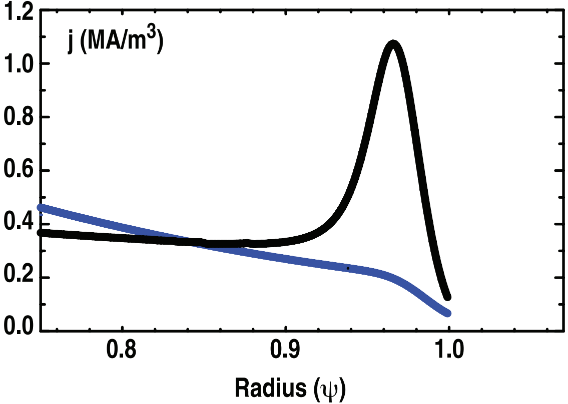

A.W. Leonard Figure 4

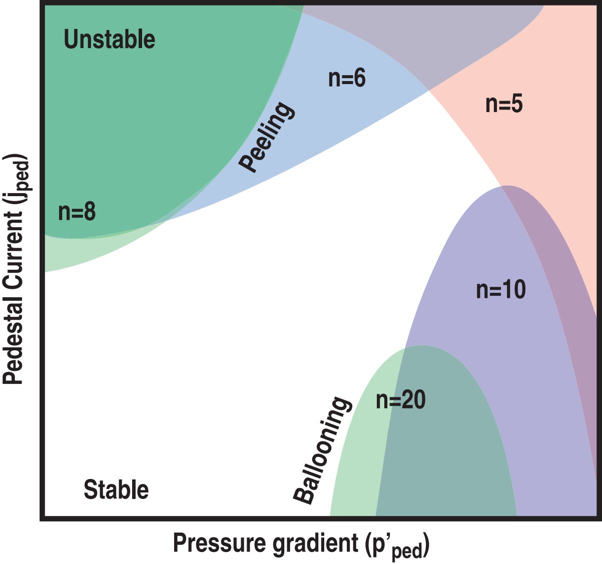

A.W. Leonard Figure 5

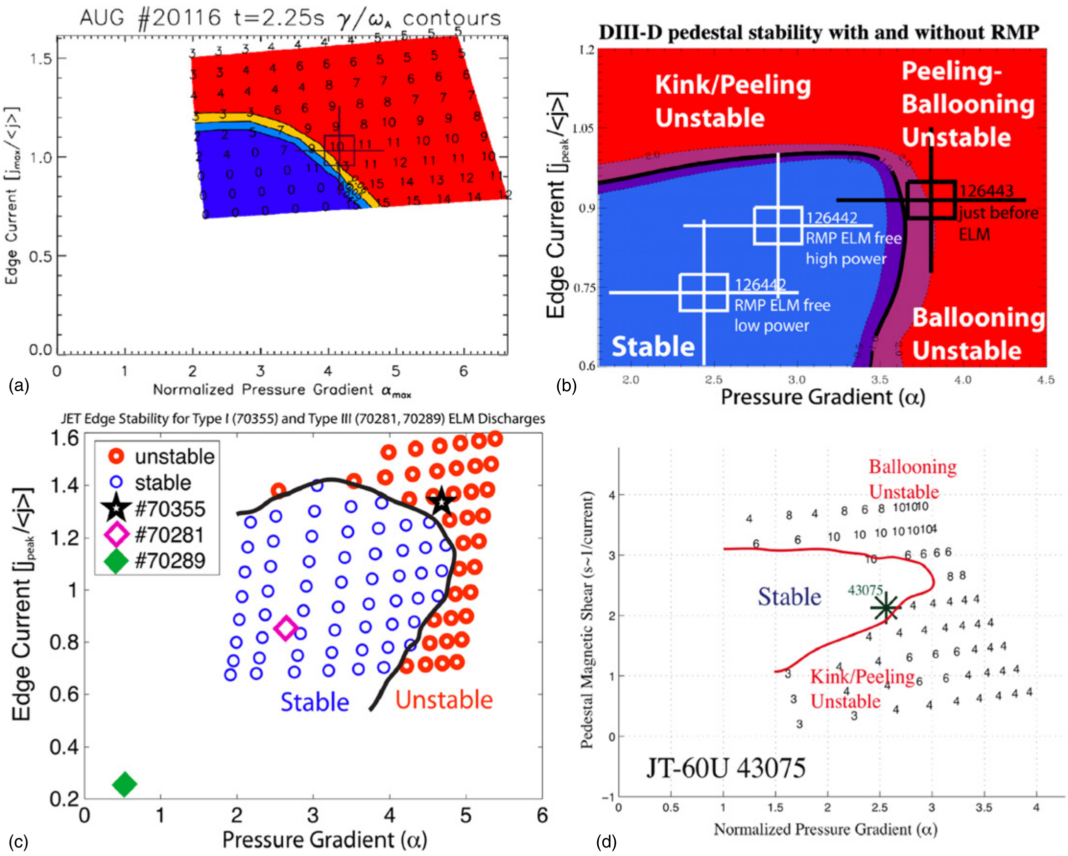

A.W. Leonard Figure 6

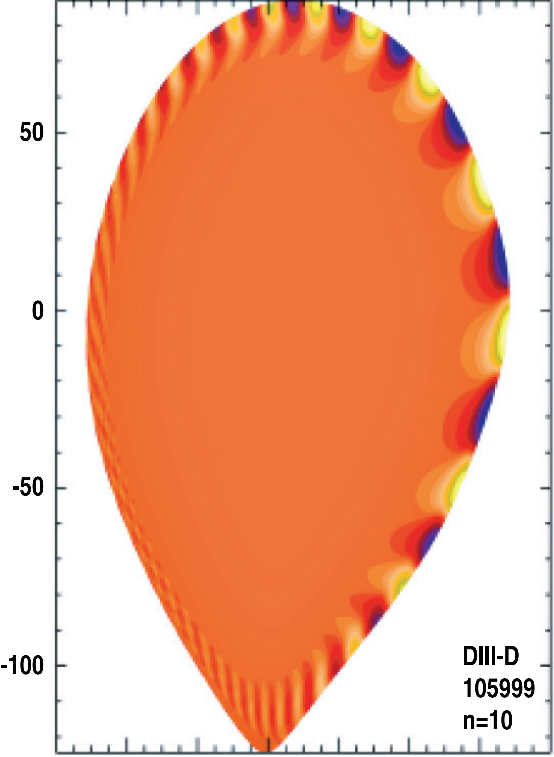

A.W. Leonard Figure 7

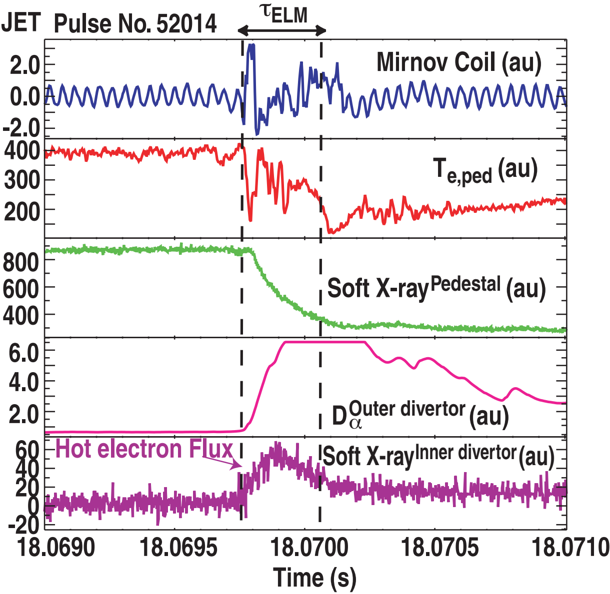

A.W. Leonard Figure 8

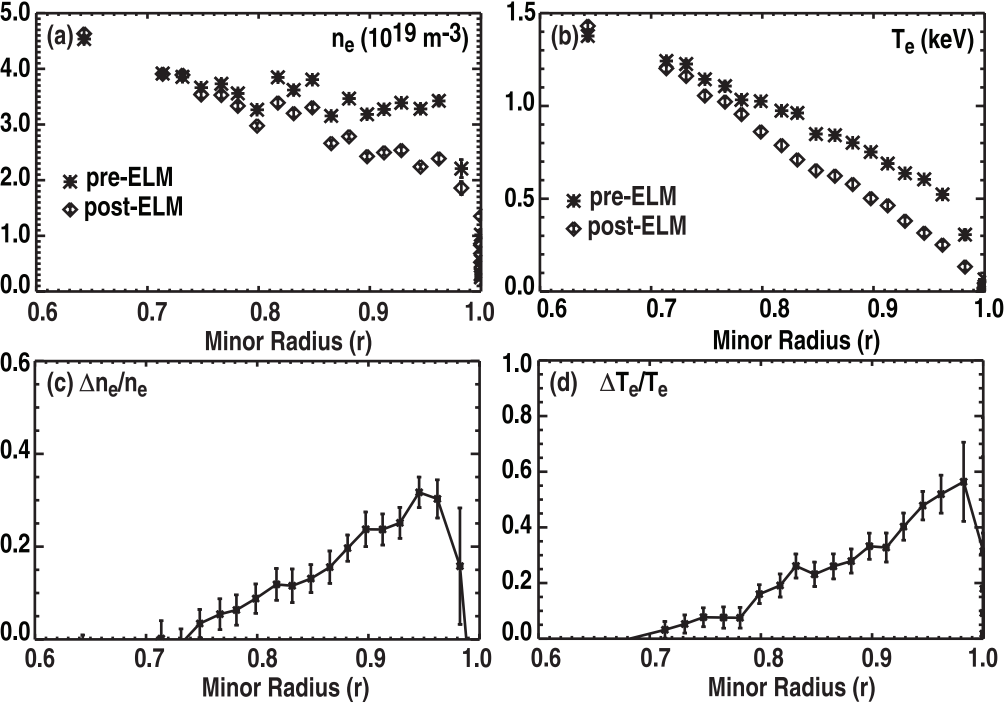

A.W. Leonard Figure 9

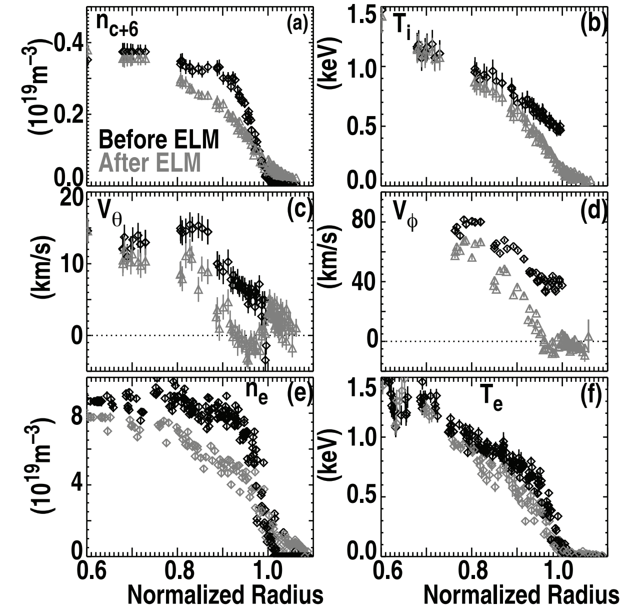

A.W. Leonard Figure 10

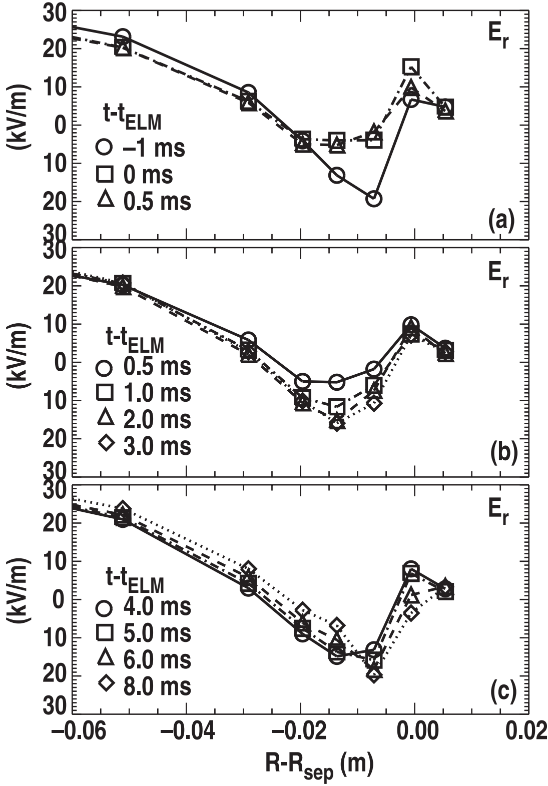

A.W. Leonard Figure 11

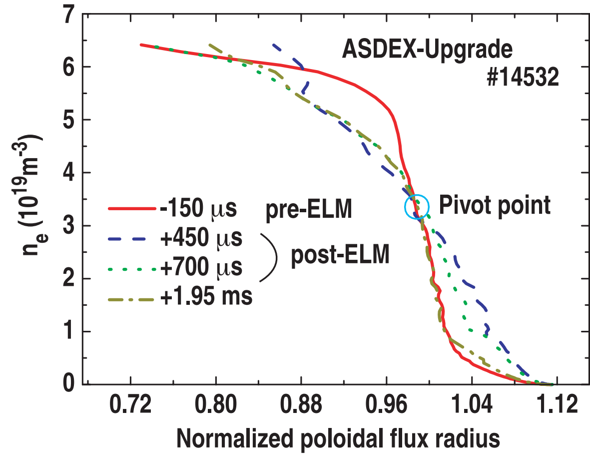

A.W. Leonard

Figure 12

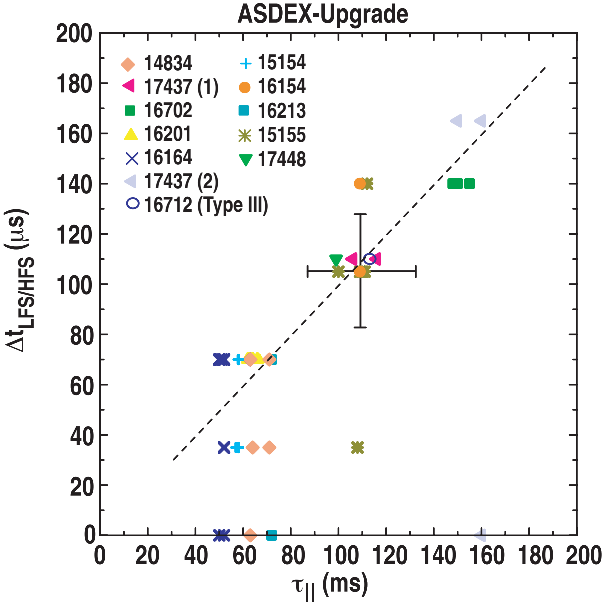

A.W. Leonard Figure 13

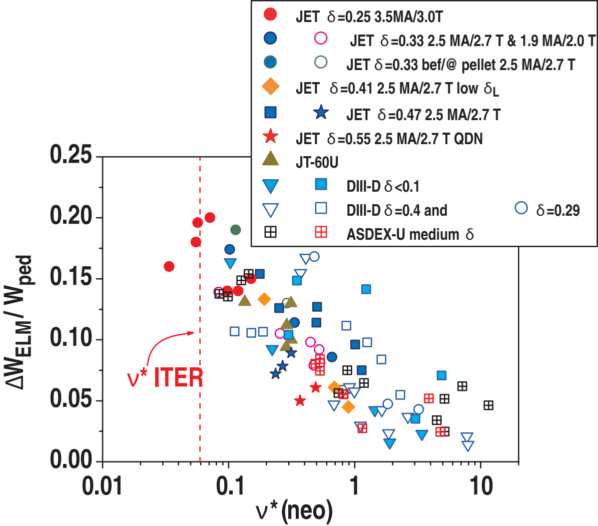

A.W. Leonard Figure 14

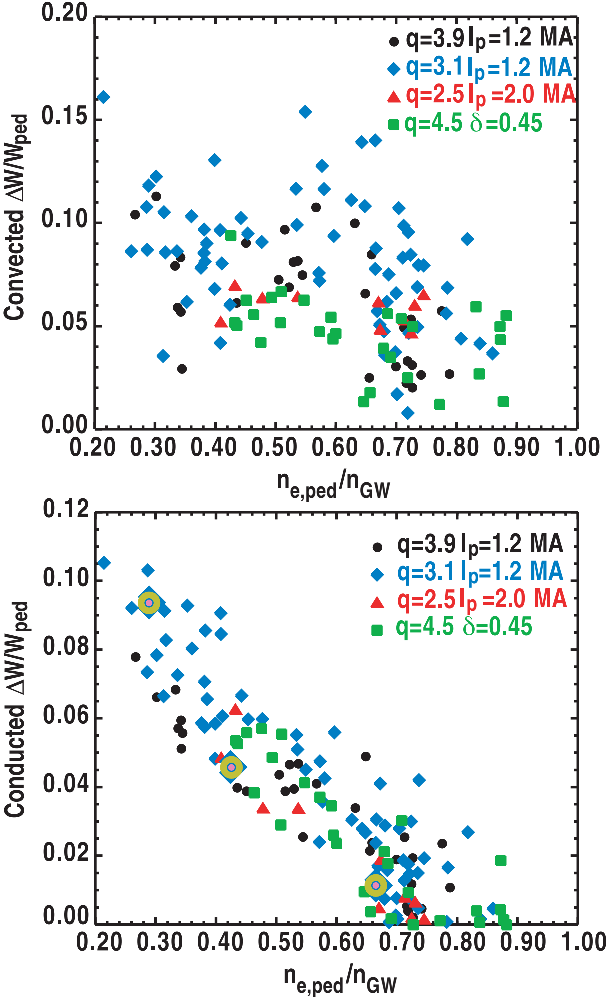

A.W. Leonard Figure 15

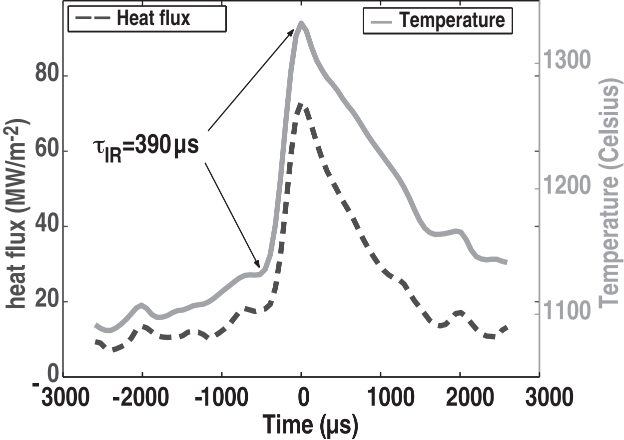

A.W. Leonard Figure 16

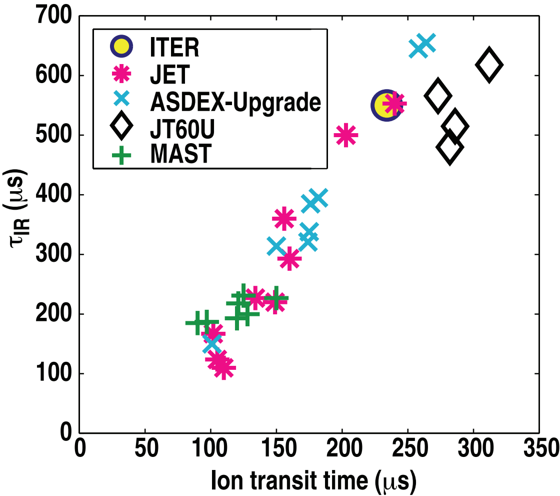

A.W. Leonard Figure 17

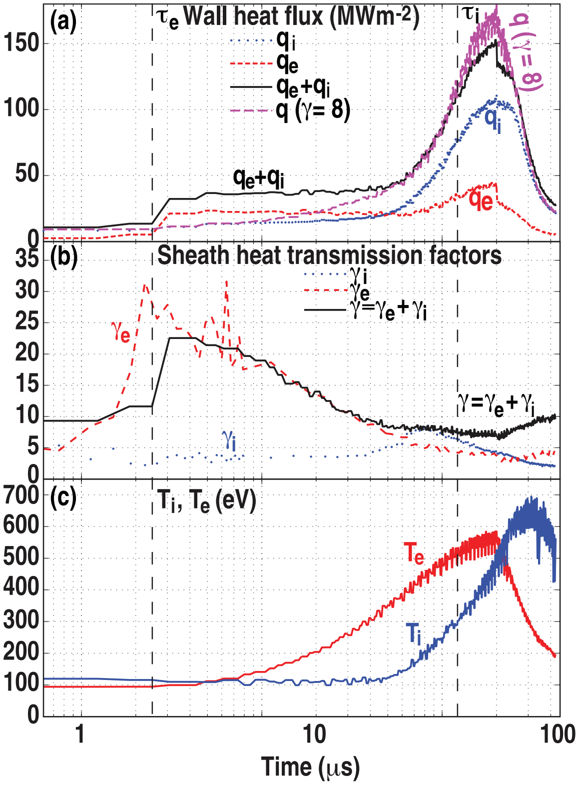

A.W. Leonard Figure 18

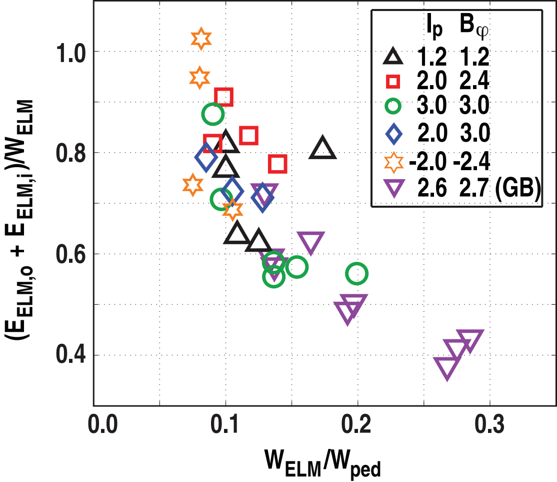

A.W. Leonard Figure 19

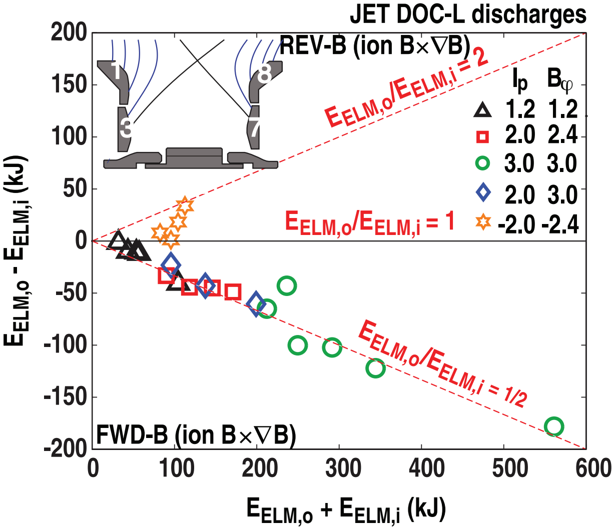

A.W. Leonard Figure 20

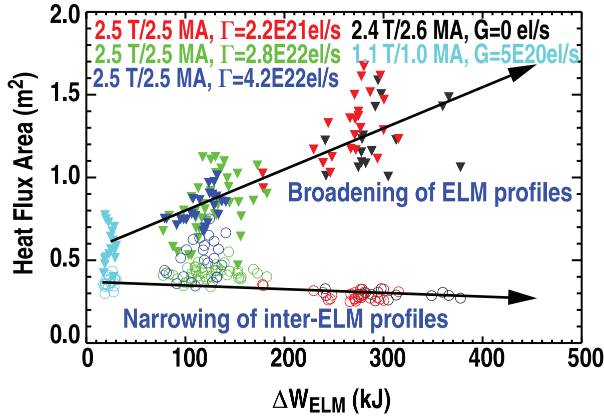

A.W. Leonard Figure 21

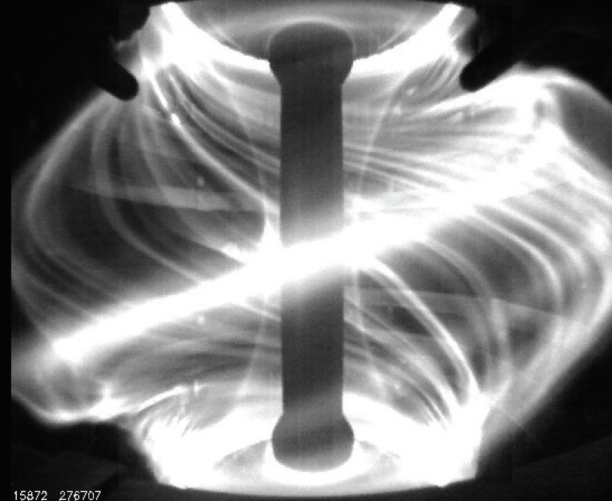

A.W. Leonard Figure 22

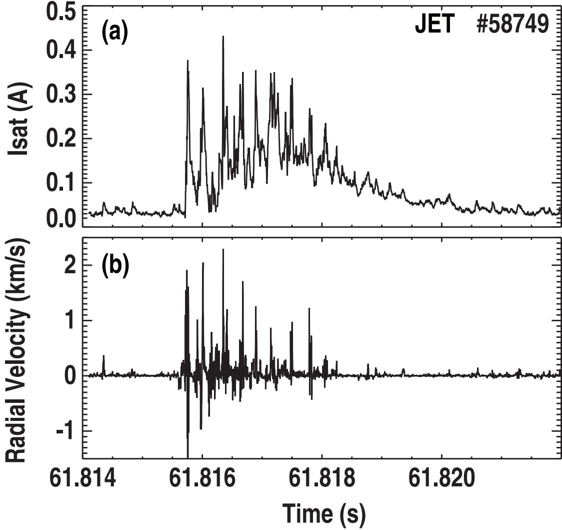

A.W. Leonard Figure 23

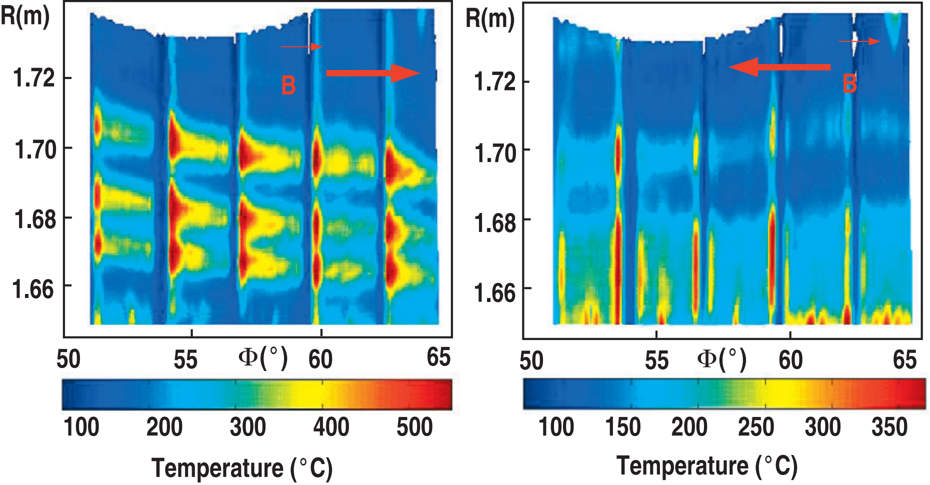

A.W. Leonard Figure 24

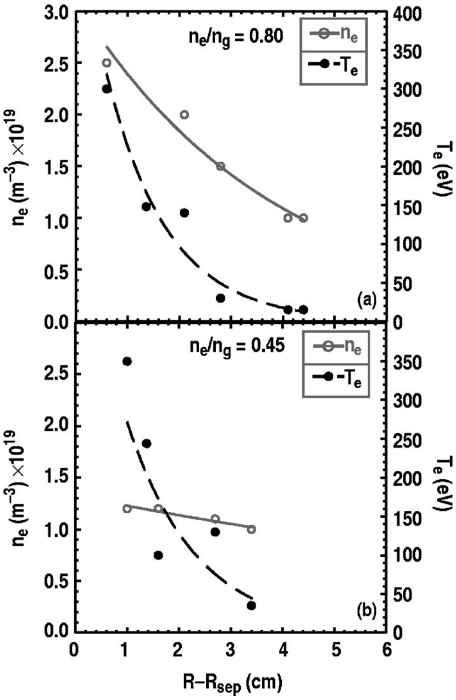

A.W. Leonard Figure 25

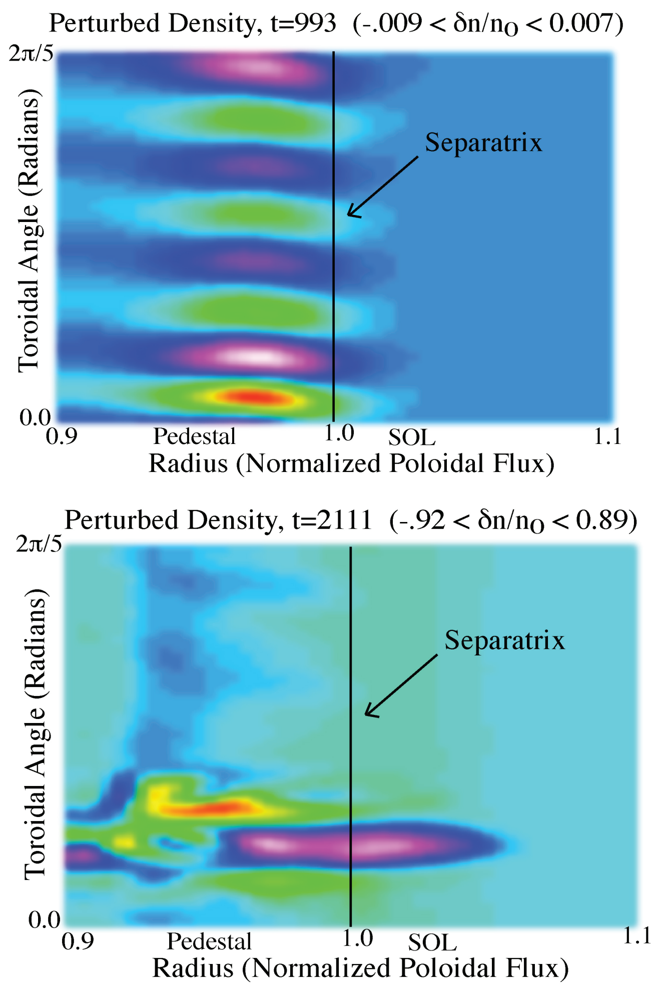

A.W. Leonard Figure 26

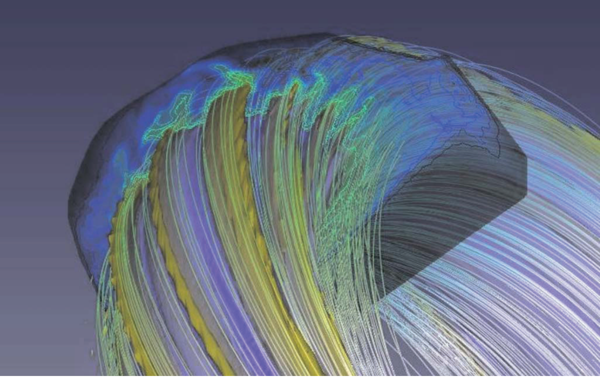

A.W. Leonard Figure 27

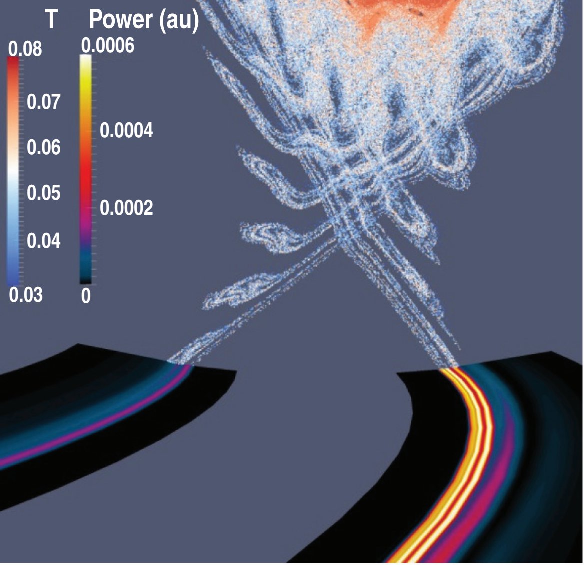

A.W. Leonard Figure 28

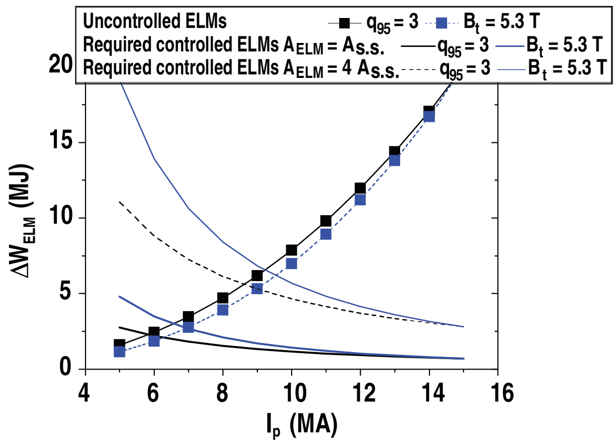

A.W. Leonard Figure 29

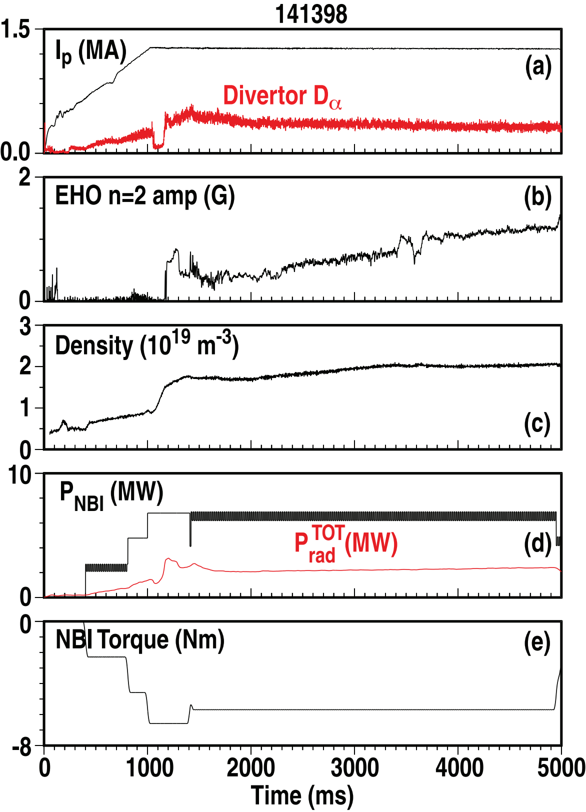

A.W. Leonard

Figure 30

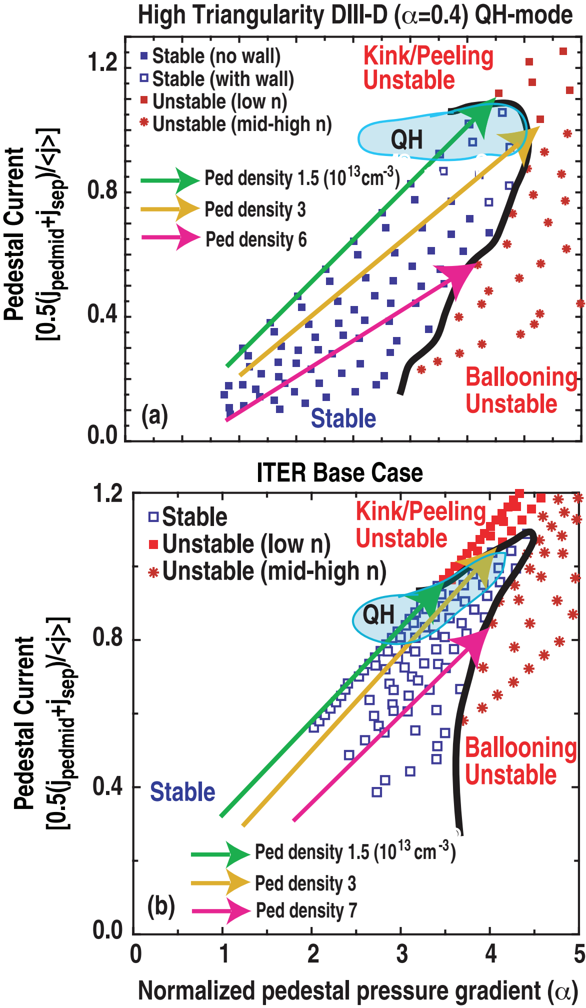

A.W. Leonard Figure 31

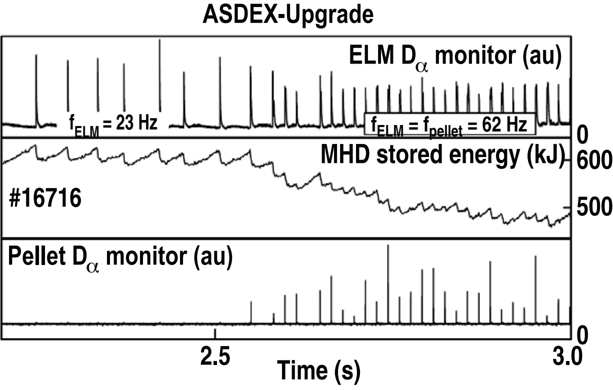

A.W. Leonard Figure 32

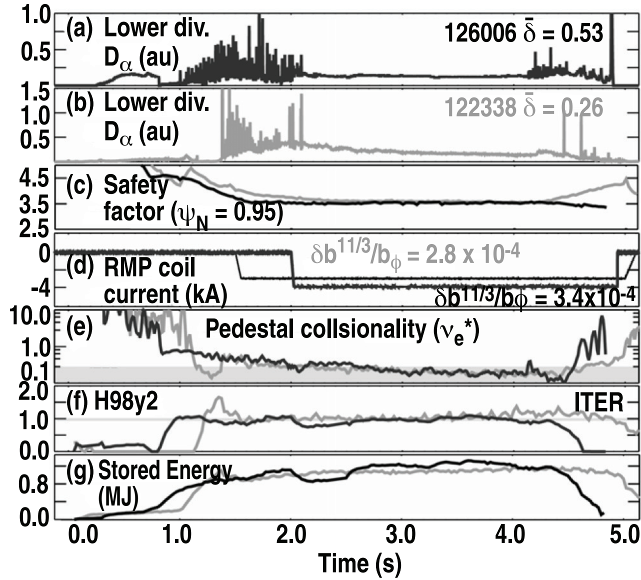

A.W. Leonard

Figure 33